Quaternary International xxx (xxxx) xxx

Contents lists available at ScienceDirect

Quaternary International

journal homepage: www.elsevier.com/locate/quaint

The earthquake environmental effects (EEEs) of the 6th February 2018, Hualien earthquake (M_W=6.4): A contribution to the seismic hazard estimation in the epicentral area

Sambit Prasanajit Naik [a], Asmita Mohanty [b], Himanshu Mittal [c], Sabina Porfido [d,e], Alessandro Maria Michetti [f], Benjamin Ming Yang [g], Ohsang Gwon [h], Young-Seog Kim [h,*]

[a] Active Fault and Earthquake Hazard Mitigation Research Institute, Pukyong National University, Busan, 48513, South Korea
[b] National Institute of Advanced Studies, Indian Institute of Sciences (IISC) Bengaluru, Karnataka, 560012, India
[c] National Center for Seismology, Ministry of Earth Sciences, Govt. of India, New Delhi, 110003, India
[d] ISA Research Council (CNR), Via Roma, 64-83100, Avellino, Italy
[e] INGV-Osservatorio Vesuviano, 80133, Napoli, Italy
[f] Dipartimento di Scienza e Alta Tecnologia, Università dell'Insubria, Via Valleggio, 11, 22100, Como, Italy
[g] Department of Geosciences, National Taiwan University, Taipei, 10617, Taiwan
[h] Department of Earth & Environmental Sciences, Pukyong National University, Busan, 48513, South Korea

ARTICLE INFO

Keywords:
EEEs
ESI-07
Hualien earthquake
Milun fault
Seismic hazard
ShakeMaps

ABSTRACT

The macroseismic intensity of the February 6, 2018, Mw 6.4, Hualien earthquake, which caused extensive damage around the Hualien area of eastern Taiwan is reassessed using the Environmental Seismic Intensity (ESI-07) scale. We compiled data on earthquake environmental effects (EEEs) caused by the 2018 Hualien earthquake, which includes surface ruptures, ground cracks, liquefaction, and occasional landslides, and estimated the epicentral intensity (I_0) as well as site-specific intensities. We found that the ESI-07 epicentral intensity of the Hualien quake in 2018 is IX. We note that the epicentral area of the 2018 Hualien earthquake was the meso-seismal area of the October 22, 1951, (M_w 6.6) Hualien earthquake, as reported in primary contemporary sources and historical earthquake catalogs. The 1951 Hualien earthquakes also caused prominent surface ruptures, liquefaction, and ground cracks. Consequently, we reassess the macroseismic intensities of this historical seismic event and compare it to the Hualien earthquake in 2018. The comparison suggests similar epicentral intensities for the two earthquakes (IX and X ESI-07). Moreover, we conducted a systematic comparison between intensity obtained using different scales which revealed the differences of two to three degrees between the ESI-07 and traditional intensity scales. This result reconfirms the significance of documentation and recording of earthquake environmental effects to make intensity assessments for modern seismic events consistent with the historical earthquake records. Moreover, a re-evaluation of historical earthquake intensity in eastern Taiwan could be performed in order to update the seismic hazard map. Application of the ESI-07 intensity scale of recent and historical earthquakes will be helpful in post-earthquake recovery efforts for a future earthquake. The prepared ShakeMaps from the ESI-07 values suggests completely different shapes to the previously generated ShakeMaps considering the peak ground acceleration or peak ground velocity. It suggests that the ShakeMaps prepared from the earthquake environmental effects can be complemented with the instrumental based intensity map to have a better seismic hazard prediction and future land use planning for the region.

1. Introduction

Macroseismic data are a valuable asset for delineation of earthquake damage distribution and earthquake source parameters for historical as well as recent earthquakes (Pettenati et al., 1999; Papanikolaou et al., 2009; Heddar et al., 2016; Nappi et al., 2017; Chunga et al., 2018). The macroseismic intensity is considered as an essential parameter for evaluating the seismic hazard by over 60% countries around the world

* Corresponding author.
E-mail address: ysk7909@pknu.ac.kr (Y.-S. Kim).

https://doi.org/10.1016/j.quaint.2022.10.009
Received 13 March 2022; Received in revised form 15 October 2022; Accepted 17 October 2022

(McGuire, 1993; Papanikolaou et al., 2009). This is may be due to the fact that the historical record and the attenuation relationship of damaging earthquakes are expressed in terms of intensity (Grandori et al., 1991), where intensity represents the direct expression of the earthquake damage and the loss estimation (Coburn and Spence, 2003). However, intensity based on the effects on the man-made environment might reflect the cultural setting and economic development rather than the strength of the earthquake (Serva, 1994; Michetti et al., 2004, 2007; Mosquera-Machado et al., 2009; Ota et al., 2009; Guerrieri et al., 2016; Huayong et al., 2019; Naik et al., 2020a). In fact, in the last decades, traditional intensity scales (MMI, MCS, JMA, CWB, and EMS-98) tend to be linked only to ground motion parameters such as peak ground acceleration (PGA) or peak ground velocity (PGV). In several countries like Japan and Taiwan, intensity assessment in the field has been almost entirely replaced by instrumental measurements. On the contrary, Earthquake Environmental Effects (in the following referred to as EEEs) are not controlled by the factors such as the effect on the man-made environment. The twelve-degree Environmental Seismic Intensity (ESI -07) scale, proposed by International Union for Quaternary Research (INQUA), solely considers the EEEs (both primary and secondary) (Michetti et al., 2007; Mosquera-Machado et al., 2009; Ota et al., 2009; Guerrieri et al., 2016; Huayong et al., 2019). The ESI-07 scale considers the size, occurrences, and aerial distribution of the EEEs, such as surface faulting, tectonic upliftment/subsidence, landslides/rock falls, liquefaction/lateral spreading, ground collapse, tsunami waves, and hydrological anomalies (Michetti et al., 2007). It assigns the seismic intensity using the quantitative analysis of these EEEs. As a result, there have been significant differences between the ESI-07 and the traditional intensities for several events around the world (Guerrieri et al., 2009; Tatevossian et al., 2010; Ali et al., 2009; Papanikolaou et al., 2009; Lekkas, 2010; Papanikolaou, 2011; Nappi et al., 2017; Chunga et al., 2018; Grützner et al., 2019) verifying that the man-made environment overshadows the traditional intensities. This kind of uncertainty can be overcome by detailed mapping of the EEEs and applying the ESI-07 scale (Michetti et al., 2007; Ota et al., 2009; Huang et al., 2019; Naik et al., 2020b). It is noticed that integration of ESI-07 and the traditional intensity scale can provide a better picture of earthquake scenarios for damaging earthquakes, more specifically for earthquakes having intensity larger or equal to IX to X, when the man-made structures are completely damaged (Huang et al., 2019). Considering this factor, the ESI-07 scale has been applied to several historical and recent earthquakes worldwide (Michetti et al., 2007; Porfido et al., 2007; Audemard et al., 2015; Porfido et al., 2015a,b; Serva et al., 2015; Serva et al., 2016; Sanchez and Maldonado, 2016; Nappi et al., 2017; Caccavale et al., 2019; Tuttle et al., 2019; Huayong et al., 2019; Porfido et al., 2020; ISPRA). Several studies suggested that the ESI-07 scale follows the same criteria–environmental effects for all earthquakes and can be comparable for earthquakes not only from different tectonic settings but also recent earthquakes with historical earthquakes (Guerrieri et al., 2009; Tatevossian et al., 2010; Ali et al., 2009; Papanikolaou et al., 2009; Lekkas, 2010; Papanikolaou, 2011; Papanikolaou and Melaki, 2017; Chunga et al., 2018; Grützner et al., 2019; Naik et al., 2020a). The association of ESI-07 with earthquake magnitude and the development of an attenuation relationship may reduce the uncertainty parameter of the attenuation relationship developed using the traditional intensity scale (Giner-Robles et al., 2015). Also, the ESI-07 scale has the objective of inclusion of paleoseismic data in macroseismic data analysis, which can extend the earthquake intensity information to a geological time scale (several years to tens of kyrs; Reicherter et al., 2009; Silva et al., 2015a, b; Papanikolaou and Melaki, 2017).

Hence, it can be inferred that the application of the ESI-07 intensity scale for a recent and historical earthquake will be helpful for a) comparison and integration with macroseismic data from traditional intensity scales, b) the preparation of refined seismic hazard maps, and c) reducing the uncertainty implied in the intensity attenuation laws (Papanikolaou, 2011; Papanikolaou and Melaki, 2017; Silva et al., 2017; Naik et al., 2020 a,b). To test the applicability of ESI-07 intensity for moderate magnitude earthquakes that occurred in a highly urbanized area with dense seismic network stations, we have reassessed the macroseismic intensity for the February 6, 2018 Hualien earthquake (Mw 6.4) in Taiwan.

Taiwan is located on the Pacific Ring of Fire and is well known for the frequent occurrence of damaging earthquakes (Fig. 1). Taiwan uses the instrumentally derived PGA or PGV values of seismic intensity measurements using the Central Weather Bureau (CWB) seismic intensity scale. But the intensity assessment using PGA or PGV is quite erratic (Wu et al., 2003). These dubious characteristics of intensity estimation can be affected by the distribution of seismic stations, the interpolation method used for the preparation of the PGA distribution map, and the heterogeneity in building codes adopted in the different parts of the country (Wu et al., 2003; Ng et al., 2011). The CWB suggests that intensity VII corresponds to severe damage or collapse of some buildings. But there are cases of earthquake collapse or damage of buildings in Taiwan for earthquakes of less than 7, i.e., during the 2016 Meinong earthquake (M_w 6.4) and the 2018 Hualien earthquake (M_w 6.4). Despite of having similar magnitude, both earthquakes caused building collapse with different recorded PGA values (Wu et al., 2019). This indicates that the earthquake intensity scale cannot depend only on the maximum recorded PGA/PGV value or other structural parameters, which may under or overestimate the seismic hazard (Wu et al., 2016, 2019).

Following the uncertainty in the observed damage pattern and seismic hazard estimation considering the PGA/PGV, this study aims to expand the existing database in Taiwan by adding new events with documented EEE for historical and recent earthquakes from eastern Taiwan. Considering the ESI-07 Intensity, ShakeMaps were prepared. The ESI-07 was compared to the intensity produced from the traditional PGA/PGV-based scales such as CWB intensity and the Modified Mercalli scale (Wood and Neumann, 1931) to test the possible systematic differences in intensity estimation. The ShakeMaps, considering the primary and secondary effects, were compared to the instrumental ShakeMaps.

2. Tectonic and geomorphic background

The 2018 Hualien (M_w 6.4) earthquake occurred near the conjugation point of the Eurasian plate and Philippine Sea plate. The Philippine Sea plate is subducting towards the northwest beneath the Eurasian

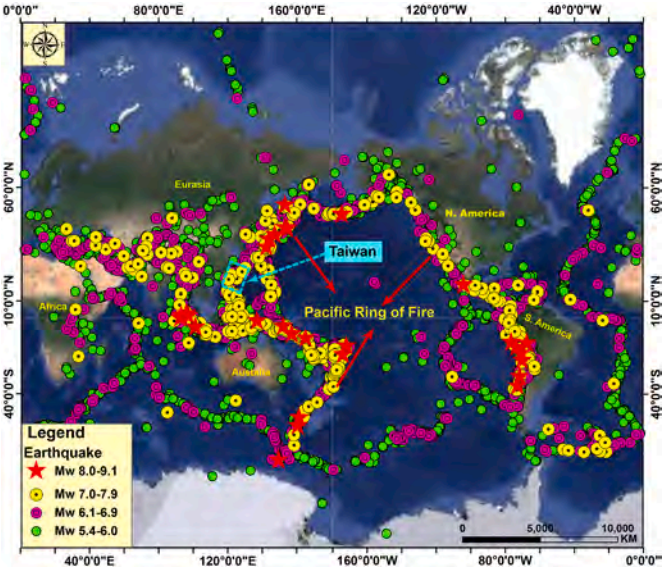

Fig. 1. Map showing the Pacific Ring of Fire and distribution of earthquakes around the Pacific Ring of Fire and its adjoining areas along with Taiwan.

plate along the Ryukyu trench, whereas the coastal range on the Philippine Sea plate collides with the Eurasian plate along the Longitudinal valley (Shyu et al., 2007; Chen et al., 2014a; Hsu et al., 2019, Fig. 2a). The GPS data show that the Philippine Sea plate moves towards NW at a rate of 82 mm yr^{-1} towards the Eurasian plate (Chen et al., 2014b; Tsai et al., 2015). This high rate of collision between the Eurasian and Philippine Sea plates resulted in a very rapid uplift of the coastal range of Taiwan. It produced several prominent tectonic features and a series of active faults. The longitudinal valley is one of the major geological structures within this collision zone (Teng, 1990; Shyu et al., 2008, Fig. 2a). Due to the ongoing collision in the eastern part of Taiwan, several active faults were developed, which are identified as the Longitudinal valley fault, Lingding fault, the northern most segment of the Longitudinal valley fault, and the Milun fault (Yu and Kuo, 2001; Lin et al., 2009; Chen et al., 2014; Yang et al., 2018; Hsu et al., 2019, Fig. 2a). The ongoing tectonic phenomena caused several destructive earthquakes along Taiwan, including the 1951 M_W 6.6 Hualien earthquake, the 1999 Mw 7.6 Chi-Chi earthquake, the 2016 M_w 6.5 Meinong earthquake during the past century (Fig. 2b; Yang et al., 2018).

Considering the analysis of aftershocks of the 2018 Hualien earthquake (CWB; Wen et al., 2019; Kuo-Chen et al., 2019), most of the aftershocks were clustered on either side of the Milun fault, which further extended towards the south along the Lingding fault (Figs. 2b and 3a). The post-earthquake field survey suggests that most of the co-seismic surface ruptures are distributed along the Milun fault and Lingding fault (Hsu et al., 2019; Huang et al., 2019). The most severely affected area during the 2018 Hualien earthquake was Hualien city, which is covered mainly by Quaternary fluvial deposits and terraces (Chung and thesis, 2003; Lin et al., 2009, Fig. 3b).

The Milun tableland is located to the east of the Milun fault (Fig. 3b). It is composed of Milun conglomerates that are covered by the Pleistocene Milun formations in the north and Milun terrace deposits in the south. The Milunshan conglomerate is composed of gravel and sand and is distributed around the Milun Hill (Fig. 3b). The Milun fault is a NE-striking and 8 km long east-dipping left-lateral strike-slip fault with a reverse component (Shyu et al., 2005; Chang et al., 2006). Recent studies (Shyu et al., 2016) suggest that the Milun fault has a slip rate of 10 mm yr^{-1} and a very short recurrence interval of 70 years. The estimated slip rate and recurrence interval for the Milun fault indicates the fault is more active than several active faults around the world, which has a recurrence interval of a few hundred years to several hundred years.

The Milun fault has produced historical earthquakes, such as the 1951 Hualien (M_W 6.6) earthquake and the 1986 Hualien (M_L = 6.8) earthquake (Chang et al., 2006). In addition to the Milun fault, the area has two minor faults; the Beipu fault and the Mingyi fault (Fig. 3b). The Beipu fault is a 2.3 km long fault located in the northwestern part of Hualien city (Hsu et al., 2019). The Mingyi fault is a west-dipping reverse fault with some strike-slip sense and is located 1 km east of the Milun fault (Lin and Hsiao, 1998; Hsu et al., 2019).

3. Seismicity around Hualien city

During the past century, the area within a 250 km radius of the 2018 Hualien earthquake epicenter has hosted 180 earthquakes of M_w 6.0+, out of which 26 events had a magnitude higher than M_w 7+ (Fig. 3a). Due to its complex tectonic setting and ongoing collision between the Philippine Sea Plate and the Eurasian plate, Hualien city has experienced several damaging earthquakes in the recent past. The historical database of the earthquakes around Hualien city indicates that several destructive earthquakes rattled the area, such as the 1920 Hualien earthquake (Ms 8.1), 1951 Hualien earthquake sequence/Longitudinal Valley earthquake (M_W 6.6–6.4), 1986 Hualien earthquake (M_W 7.3) and the recent 2018 Hualien earthquake (M_w 6.4) (Fig. 2b; Fig.3a; Wang and Kuo, 1995; Lee et al., 2008; Yang et al., 2018; Chen et al., 2019). In 1920, an earthquake occurred around 50 km east of Hualien city and was known as the 1920 Hualien earthquake (Fig. 2b). This was Taiwan's largest ever recorded earthquake (Wang and Kuo, 1995; Theunissen et al., 2010). The exact faulting mechanism involved in this earthquake remains unclear. Despite being the largest recorded earthquake in Taiwan, the earthquake was not so devastating as other earthquakes, such as the 1999 Chi-Chi earthquake. The earthquake caused 8 deaths, 24 injuries, and some building damage around the most populated areas in Taiwan, such as Taipei, Taoyuan, Hsinchu, and Taitung, which highlights the seismic risk in Taiwan.

The 1951 Longitudinal valley fault earthquake sequence was one of

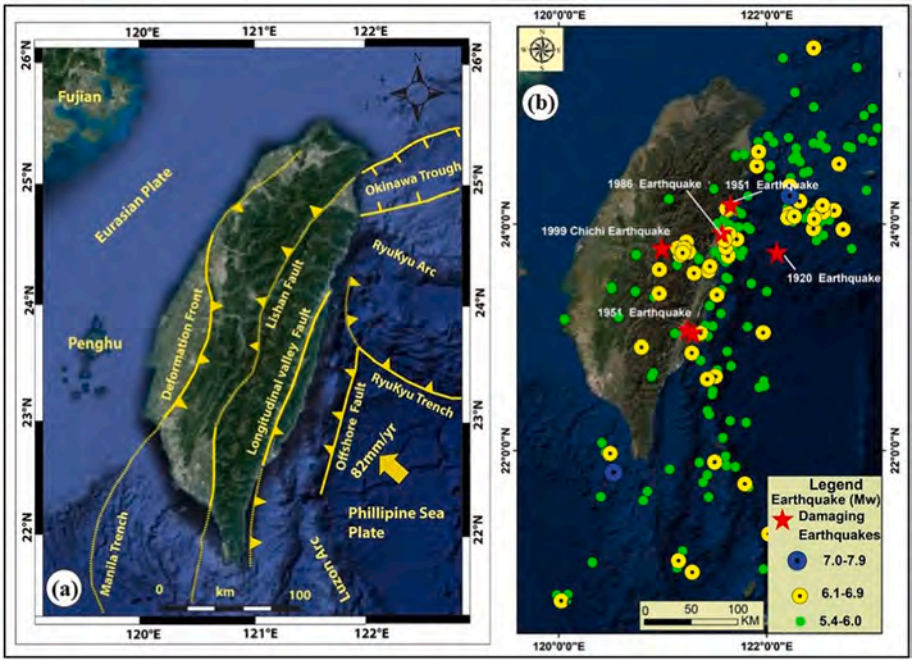

Fig. 2. (a) Simplified map of the tectonic setting in Taiwan with major faults. (b) Distribution of earthquake epicenters on and around Taiwan (between 1986 and 2015).

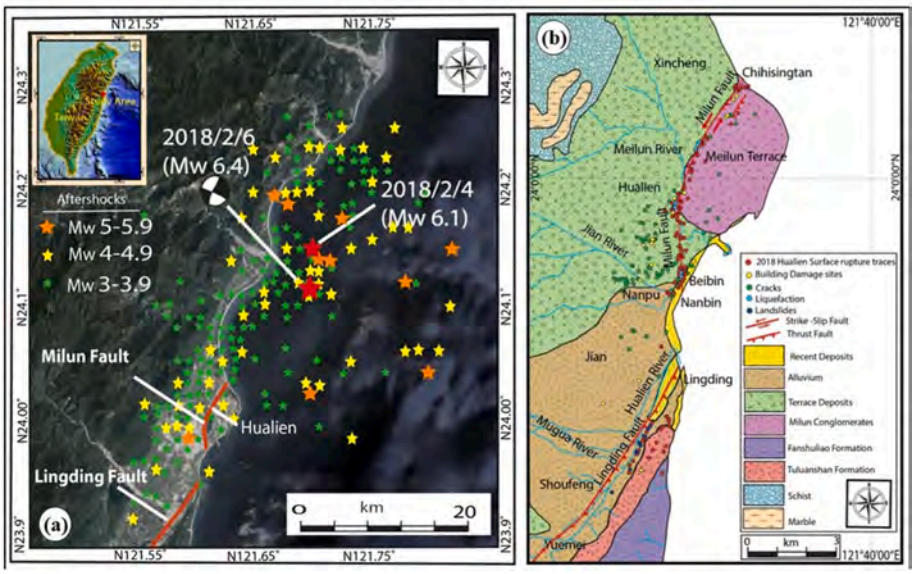

Fig. 3. (a) Map showing the location of 2018 Hualien earthquake main shock and its aftershock along the Lingding and Milun Fault. (b) Simplified geological map showing the Milun fault, Lingding Fault, which are the major active faults located around the epicentral area and experienced surface rupture during both the earthquakes (Modified from Lin et al., 2009; Hsu et al., 2019). Different colored dotted features indicate the ground effects caused by the 2018/02/06 Hualien earthquake along the Lingding fault and the Milun fault.

the most damaging seismic events in eastern Taiwan, which caused over 80 fatalities and destroyed several lifeline structures (Fig. 2b). The Longitudinal Valley earthquake sequence includes 12 earthquakes of M_L > 6.0 covering around ~150 km stretch of Longitudinal valley between 22nd October to December 5, 1951 (http://scman.cwb.gov.tw/eqv5/10eq/10eqindex.htm; Cheng et al., 1996; Lo et al., 2013). Out of 12 M_L > 6.0 earthquakes, three earthquakes occurred on the 22nd of October around the harbor city of Hualien at the northern tip of the Longitudinal Valley Fault and had magnitude M_L >7 (Cheng et al., 1996; Lo et al., 2013). The first event occurred around 05:34 a.m., with a magnitude of M_L 7.3/M_W 6.6 (epicentral location- 23.875°N-121.725°E, depth 4 km). The second event occurred at 11:29 a.m. with a magnitude of M_L7.1/M_W 6.4 (epicentral location 24.075°N/121.725°E) with a focal depth of 1.0 km. Due to its shallow depth, it caused extensive surface rupture and damage around Hualien city (Cheng et al., 1996; Cheng et al., 1996; Lo et al., 2013). The third event occurred around 1:43 p.m. with a magnitude of M_L7.1/M_W 6.4 (epicentral location 23.825°N −121.950°E). The focal depth of the third event was around 18 km. The local magnitude (M_L) of the 1951 earthquake sequences was converted to the moment magnitude (M_W) as per the empirical formula provided by Huang et al. (2000). The October 22, 1951 earthquake report issued by the Taiwan Weather Bureau in 1952 suggested the Milun fault near Hualien generated a ~9–10 km long rupture during the 1951 earthquake. Lee et al. (2008) measured the horizontal offset using geodetic observations and suggested that the earthquake caused a maximum horizontal offset of around 4 m (Table S1). During the October 22, 1951 Longitudinal valley fault earthquake, the Milun fault caused a 2 m sinistral offset and 1.2 m vertical uplift (Taiwan Weather Bureau, 1952; Yang, 1953; Cheng et al., 1996; Cheng et al., 1996; Chung and thesis, 2003; Shyu et al., 2007; Lee et al., 2008, Fig. 2). The Longitudinal Valley earthquake sequence on 24th November caused a ~70 km long surface rupture towards the northern part of the Longitudinal Valley (Taiwan Weather Bureau, 1952; Hsu, 1961; Chung and thesis, 2003; Huang et al., 2019, Fig. 4). Shyu et al. (2007), divided the surface rupture into three segments. The Chihsang rupture length was 30 km long, whereas the Yuli fault rupture and the Rueisuei Fault rupture were about 20 km and 15 km long, respectively. Several photographs are available in the historical records for the 1951 earthquake showing the surface ruptures. However, ambiguity remains regarding the exact location of the surface breaks, as most of the documented photographs focused their attention on overturned houses rather than surface break-up traces. Based on archived field photos and newspapers, the surface rupture extended to the old Hualien city (Cheng et al., 1996; Chung and thesis, 2003; Shyu et al., 2007; Lin et al., 2009). The CWB reported the maximum macroseismic intensity of VI in the Taiwan intensity scale based on documented damage, which includes PGA values of more than 0.25 g and evidence of surface rupture, landslides, and house damages during the earthquake (Cheng et al., 1996; Fig. S1).

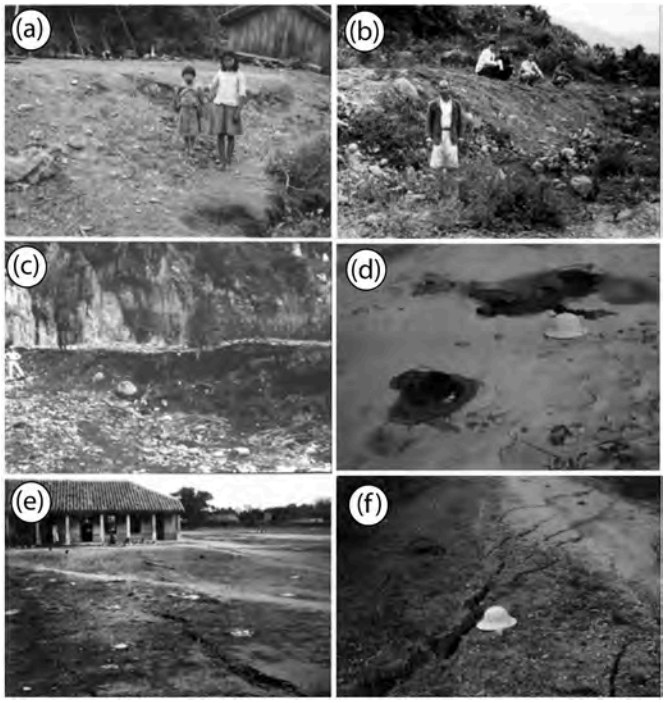

Fig. 4. Field photographs showing (a) 1.2 m vertical fault scarp at the southeast of Fuyuan, Ruisui town, (b) 2 m high scarp near Dafu, Hualien county (c) 1.50 m high fault scarp observed near Ruisui Town, Hualien county, (d) sand boil observed near Sanmin, (e) 15–20 cm wide ground cracks observed at Yuli National School, Yuli, Hualien (f) The cracks observed in the road between Dongli and Dongzhu, Hualien city during 1951 Longitudinal valley earthquake (Photographs are taken from Chung and thesis, 2003).

On November 14, 1986, an earthquake occurred around 20 km east of Hualien (Fig. 2b). The focal depth of the earthquake was 15 km, and the magnitude was M_W 7.3 (Chen et al., 2019). The earthquake shook

Taiwan and Penghu Islands, causing 15 deaths and 62 injuries. About 37 houses collapsed, and more than 200 buildings were damaged (Tsai and Thesis, 1987). The earthquake caused severe amplification effects around Hualien city as far as 120 km from the epicenter. There were no primary effects reported for this earthquake.

The 2018/02/06 Hualien earthquake (M_W 6.4) originated near the shoreline close to Hualien city with a hypocenter depth of about 6.3 km. The epicenter was located 18.3 km north-northeast of the city of Hualien, with most of the rupture extending offshore (Wu et al., 2019, Fig. 3a). The moment tensor plot and clustering of aftershock show that the earthquake had a dominant strike-slip motion with NE-SW strike and NW dip. During the 2018 Hualien earthquake, maximum shaking intensity of VII in the instrumental intensity scale that is presently used in Taiwan was observed around Hualien city and Ilan city (Kuo-Chen et al., 2019; Hsu et al., 2019; Huang et al., 2019; Wu et al., 2019). The earthquake caused considerable structural damage with ~300 causalities (CGS, 2018; Kuo-Chen et al., 2019; Wu et al., 2019; Lin et al., 2020).

From this, it can be inferred that despite the repeated occurrence of damaging earthquakes around Hualien city, detailed documentation of the earthquake-induced ground effects has been recorded for only a few earthquakes, such as the 1951 Longitudinal Valley earthquakes. But several researchers reported the ground effects caused by the 2018/02/06 Hualien earthquake using field mapping, UAV techniques, and InSAR techniques. These datasets were used for the ESI-07 intensity assignment and generation of Shake Map in this paper.

4. Earthquake environmental effects (EEEs) of 2018 Hualien earthquake

The 2018 Hualien earthquake caused extensive primary and secondary effects around Hualien city (Fig. 3b; Fig. 5). The primary effects include surface ruptures, whereas the observed secondary effects were liquefaction, ground cracks, ground subsidence, and rockfalls around the epicentral area. The earthquake produced a 9–15 km long (CGS, 2018) surface rupture along the Milun fault during the mainshock. The observed surface rupture was quite surprising as its location is not projected along the strike of the estimated hypocenter of the mainshock. The post-earthquake field survey accompanied by an aerial survey showed that the surface rupture was observed along the northern part of the Milun fault with maximum sinistral offset (≤70 cm), whereas the southern part of the Milun fault showed less sinistral offset (~5–15 cm) (CGS, 2018; Lin et al., 2019; Kuo et al., 2019; Huang et al., 2019; Hsu et al., 2019). Any post-earthquake survey team does not demarcate the offshore extension of the surface rupture. The quantitative information for both primary and secondary effects was collected from various sources in this paper and used for the macroseismic intensity assessment using the ESI-07 intensity scale. Also, the assessed ESI-07 values were compared with the other seismic intensity scales.

4.1. Primary effects

The primary effects associated with the 2018 Hualien earthquake are mostly surface ruptures confined along the previously mapped Milun fault and the northernmost part of the Lingding fault (Figs. 3b and 5). The presence of the previously mapped Milun fault controls the distribution and amount of surface rupture (Fig. 3b, Fig. S2). The 2018 Hualien earthquake generated a ~7.5 km long trace of surface rupture along the Milun fault (Fig. 5; Table 1). The surface ruptures of the 2018 Hualien earthquake do not show a single plane rupture like other strike-slip faults worldwide (McClay and Bonora, 2001; Klinger, 2010). It shows distributed deformation along the fault. The post-earthquake field mapping suggests that the surface rupture shows en echelon tension cracks, tension fractures, conjugate shear fractures, and compression textures along the Milun fault (Lin et al., 2019; Kuo et al., 2019; Hsu et al., 2019; Huang et al., 2019).

The northernmost location of the surface rupture occurred along the

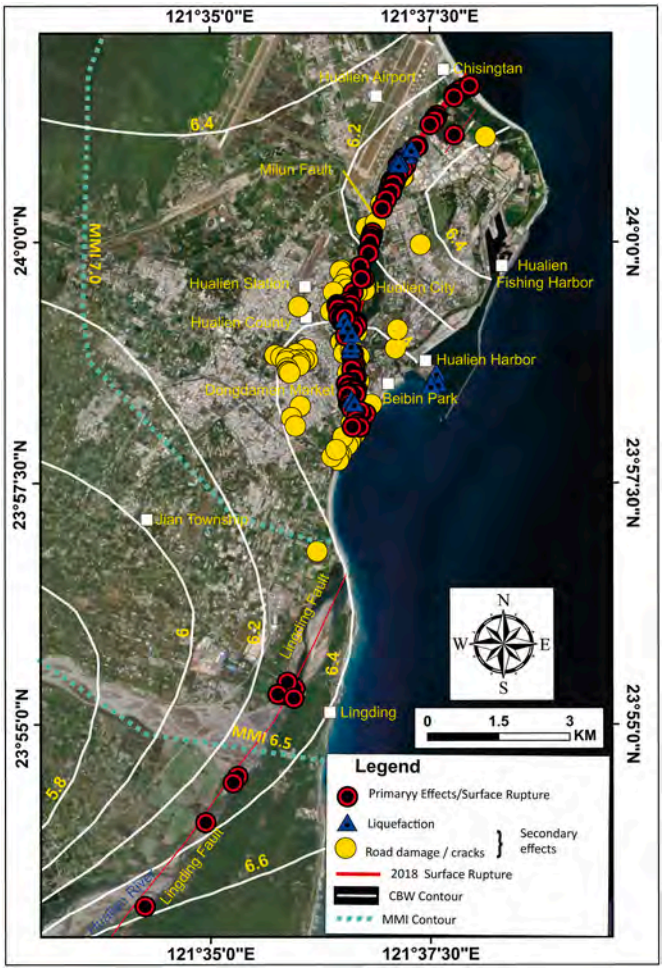

Fig. 5. Map showing the distribution of primary and secondary effects of the February 6, 2018 Hualien earthquake taken for this study. The white solid line shows the CWB intensity contour of the 2018 Hualien earthquake and light green dotted line shows the MMI contour (Intensity contour data were taken from, CWB, 2018: https://scweb.cwb.gov.tw/en-us/earthquake/ShakeMaps/ee20180206235041620 22 and USGS: https://earthquake.usgs.gov/earthquakes/eventpage/us700038c1/executive). Image source: Esri, Digital Globe, Geo Eye, i-cubed, USDA FSA, USGS, AEX, Get mapping, Aero grid, IGN, IGP, Swiss topo, and the GIS User Community. (For interpretation of the references to color in this figure legend, the reader is referred to the Web version of this article.)

Chihsingtan Beach area, where a 30 cm sinistral offset with a 20 cm vertical offset was observed (Table 1; Huang et al., 2019; Hsu et al., 2019). The strike of the surface rupture is N60°E. Near Chihsing Street, the maximum offset of 77 cm sinistral offsets with 40 cm uplift was observed along the northern segment of the Milun fault (Table 1). The surface rupture further extends towards the south along Mount Chihsing, where the rupture shows a 70 cm sinistral offset with a 40 cm extension. Near the Chihsingtan Bridge, the fault shows a 70 cm of sinistral offset. Towards further south, the surface rupture extends along a pre-existing scarp with a strike of N37°E, and it has a cumulative offset of 70 cm and uplift of 50 cm, respectively. Along this segment, the fault shows complex rupture phenomena. Near Huashi Street, the rupture produced several NW striking shear cracks and a 70 cm sinistral offset. To more south, near the National Dong Hwa University, the rupture bifurcated into two segments where the sinistral offset varies from 7 cm to 15 cm (Fig. 6; Table 1).

The trace of surface rupture with a strike of N24°E was observed further south until Mount Meilun. On the west side of Mt. Meilun, near the intersection point of Shangzhi road and Xinxing road, the

Table 1
The measured surface rupture data around Chihsingtan Beach, north Meilun, around Mt. Meilun, and around downtown of Hualien (measurements are taken from CGS, 2018; Huang et al., 2019, MM intensity from were taken from USGS, last accessed January 10, 2022; CWB intensity values were taken from Central Weather Bureau, Seismological Division, Taiwan, last accessed January 10, 2022).

Sl. No	Latitude	Longitude	Type of Displacement	Surface rupture dimensions (Length in cm, Horizontal offset and Vertical offset in cm)	Intensity		
					Esi-07	CWB	MM
1	24.027063	121.632576	Reverse/Sinistral	2500 cm long, 10 cm sinistral,20 cm uplift	IX	VII	VII
2	24.026881	121.632686	Sinistral	2000 cm long,30 cm sinistral	IX	VII	VII
3	24.026831	121.632139	Sinistral	500 cm long,30 cm sinistral	IX	VII	VII
4	24.026743	121.63193	Sinistral	Few cm horizontal offset	VIII	VII	VII
5	24.026752	121.631977	Sinistral	Few cm horizontal offset	VIII	VII	VII
6	24.026757	121.632072	Sinistral	Few cm horizontal offset	VIII	VII	VII
7	24.026773	121.632129	Sinistral	Few cm horizontal offset	VIII	VII	VII
8	24.026742	121.632035	Dextral/Tension	10 cm horizontal and 5 cm tension	VIII	VII	VII
9	24.026728	121.632058	Sinistral/Tension	Few cm sinistral off set with 5 cm extension	VIII	VII	VII
10	24.026819	121.632233	Sinistral	3,50 cm length with 10 cm sinistral offset	IX	VII	VII
11	24.026773	121.632263	Dextral	500 cm length with 50 cm dextral offset	IX	VII	VII
12	24.026712	121.631749	Sinistral/Reverse	25 sinistral offset with 40 cm vertical offset	IX	VII	VII
13	24.026686	121.631681	Sinistral	70 cm sinistral offset	IX	VII	VII
14	24.025584	121.629982	Sinistral	70 cm sinistral offset	IX	VII	VII
15	24.025556	121.629909	Sinistral	30 cm compression	VIII	VII	VII
16	24.026484	121.631245	Reverse/sinistral	27 cm vertical offset	VIII	VII	VII
17	24.026165	121.630815	Tensional fracture	40 cm tension	VIII	VII	VII
18	24.026195	121.630586	Tension	5 cm tension	VIII	VII	VII
19	24.025584	121.629982	Sinistral	70 cm horizontal offset	VIII	VII	VII
20	24.025556	121.629909	Sinistral	Few cm sinistral offset with 30 cm compression	VIII	VII	VII
21	24.025517	121.629677	Tension	Few cm sinistral offset with 10 cm extension	VIII	VII	VII
22	24.025517	121.629677	Tension	Few cm sinistral offset with 10 cm extension	VIII VIII	VII	VII
23	24.025469	121.629595	Dextral	1 cm dextral offset	VIII	VII	VII
24	24.025337	121.629687	Tension	30 cm tensional cracks	VIII	VII	VII
25	24.025085	121.629606	Compression	70 cm compressional cracks	VIII	VII	VII
26	24.021888	121.62636	Compression	5 cm compressional cracks along the surface rupture	VIII	VII	VII
27	24.021465	121.626185	Compression	10 cm Compression	VIII	VII	VII
28	24.021455	121.626175	Compression	50 cm Compression	VIII	VII	VII
29	24.021383	121.625869	Compression	5 cm Compression	VIII	VII	VII
30	24.021141	121.625953	Sinistral/Tension	23 cm sinistral offset with 15 cm tensional cracks	VIII	VII	VII
31	24.021054	121.625877	Uplift	50 cm vertical off set	IX	VII	VII
32	24.020326	121.625057	Sinistral	Few cm sinistral offset	VIII VIII	VII	VII
33	24.016603	121.622564	Sinistral/Tension	Few cm sinistral offset	VIII	VII	VII
34	24.01658	121.622711	Sinistral	10 cm sinistral offset	VIII	VII	VII
35	24.01658	121.622711	Sinistral	10 cm sinistral offset	VIII	VII	VII
36	24.016455	121.622434	Sinistral	>1000 cm long, 10 cm sinistral offset, 10 cm vertical offset, 5 cm wide	IX	VII	VII
37	24.014564	121.619973	Uplift	30 cm vertical offset	IX	VII	VII
38	24.013462	121.619057	Compression	3 cm wide compressional cracks	VIII	VII	VII
39	24.01339	121.618996	Sinistral/Reverse	100 cm long, 20 cm sinistral offset,10 cm vertical offset	IX	VII	VII
40	24.013272	121.619098	Uplift	3 cm vertical offset	VIII	VII	VII
41	24.013264	121.619086	Compression	5 cm compression	VIII	VII	VII
42	24.012193	121.619155	Sinistral	6 cm sinistral offset	VIII	VII	VII
43	24.011993	121.619149	Tension	5 cm vertical offset,15 cm tension	VIII	VII	VII
44	24.011808	121.61893	Tension	10 cm tension	VIII	VII	VII
45	24.011713	121.618885	Tension	5 cm tension	VIII	VII	VII
46	24.010671	121.617843	Tension	22 cm tension	VIII	VII	VII
47	24.0106	121.617807	Tension	10 cm tension	VIII	VII	VII
48	24.010475	121.617702	Tension	5 cm tension	VIII	VII	VII
49	24.01855	121.6296	Tension	1 cm tension	VIII	VII	VII
50	24.013266	121.620428	Sinistral/Tension	6 cm sinistral offset,5 cm tension	VIII	VII	VII
51	24.012656	121.619851	Sinistral/Tension	5 cm tension	VIII	VII	VII
52	24.011537	121.618905	Sinistral/Tension	6 cm sinistral offset, 5 cm tension	VIII	VII	VII
53	24.010673	121.618428	Sinistral/Reverse	2 cm sinistral offset with 5 cm vertical offset	VIII	VII	VII
54	24.010595	121.618443	Sinistral/Tension	Few cm sinistral offset with 5 cm tension	VIII	VII	VII
55	24.010454	121.617747	Tension	18 cm wide tensional cracks	VIII	VII	VII
56	24.010454	121.617747	Tension	6 cm	VIII	VII	VII
57	24.010454	121.617747	Tension	10 cm	VIII	VII	VII
58	24.010384	121.618291	Dextral	5 cm dextral offset 3 cm tension	VIII	VII	VII
59	24.010384	121.618291	Sinistral/Tension	Few cm sinistral offset with 3 cm tension	VIII	VII	VII
60	24.010327	121.618074	Tension	5 cm tension	VIII	VII	VII
61	24.010117	121.61762	Tension	25 cm tension	VIII	VII	VII
62	24.010081	121.618155	Tension	5 cm tension	VIII	VII	VII
63	24.009195	121.61786	Sinistral	7 cm sinistral offset with 1 cm tension	VIII	VII	VII
64	24.009093	121.617778	Dextral/Tension	1–4 cm sinistral offset with 5 cm tension	VIII	VII	VII
65	24.009061	121.617348	Compression	10 cm compression	VIII	VII	VII
66	24.008943	121.617764	Dextral/Tension	1 cm dextral offset with 5 cm tension	VIII	VII	VII
67	24.008875	121.617317	Sinistral	8 cm sinistral offset	VIII	VII	VII
68	24.008875	121.617317	Dextral	5 cm dextral offset	VIII	VII	VII

(*continued on next page*)

Table 1 (*continued*)

Sl. No	Latitude	Longitude	Type of Displacement	Surface rupture dimensions (Length in cm, Horizontal offset and Vertical offset in cm)	Intensity		
					Esi-07	CWB	MM
69	24.008875	121.617317	Compression	15 cm compression	VIII	VII	VII
70	24.008787	121.617722	Dextral	1 cm dextral,1 cm tension	VIII	VII	VII
71	24.008674	121.61769	Dextral	2 cm dextral, 1 cm tension	VIII	VII	VII
72	24.007555	121.616771	Sinistral/Compression	20–30 cm sinistral offset with 5 cm compression	VIII	VII	VII
73	24.007555	121.616771	Sinistral	30 cm sinistral offset	IX	VII	VII
74	24.007397	121.616724	Sinistral/Tension	20 cm sinistral offset, 20 cm tension	IX	VII	VII
75	24.005821	121.615955	Tension	200–300 cm long, 6 cm tension	IX	VII	VII
76	23.98566	121.6092	Tension	5 cm tension	VIII	VII	VII
78	23.98574	121.6092	Tension	2 cm tension	VIII	VII	VII
79	23.986	121.6091	Tension	1 cm tension	VIII	VII	VII
80	23.98627	121.6083	Compression	13 cm compression	VIII	VII	VII
81	23.98623	121.6087	Compression	21 cm	VIII	VII	VII
82	23.98618	121.609	Tension	7 cm tension	VIII	VII	VII
83	23.98613	121.609	Tension	2 cm tension	VIII	VII	VII
84	23.98644	121.6088	Tension	5 cm vertical offset, 5 cm tension	VIII	VII	VII
85	23.98642	121.6088	Tension	3 cm tension	VIII	VII	VII
86	23.9863	121.6089	Tension	6 cm tension	VIII	VII	VII
87	23.98628	121.6089	Tension	3 cm tension	VIII	VII	VII
88	23.98682	121.6088	Tension	3 cm vertical offset,3 cm tension	VIII	VII	VII
89	23.98681	121.6085	Tension	1.5 cm tension	VIII	VII	VII
90	23.98677	121.6086	Tension	3 cm vertical offset,3 cm tension	VIII	VII	VII
91	23.98671	121.6086	Tension	6 cm vertical offset,6 cm tension	VIII	VII	VII
92	23.98668	121.6086	Tension	7 cm vertical offset,7 cm tension	VIII	VII	VII
93	23.98647	121.6087	Tension	5 cm vertical offset,5 cm tension	VIII	VII	VII
94	23.98682	121.6088	Tension	4 cm vertical offset,4 cm tension	VIII	VII	VII
95	24.0016	121.6141	Tension/Sinistral	Few cm sinistral, 2 cm tension	VIII	VII	VII
96	24.0016	121.6141	Tension/Sinistral	Few cm sinistral, 9 cm tension	VIII	VII	VII
97	24.0016	121.6141	Tension/Sinistral	Few cm sinistral, 12 cm tension	VIII	VII	VII
98	24.0016	121.6141	Tension/Sinistral	Few cm sinistral, 1.5 cm tension	VIII	VII	VII
99	24.0016	121.6141	Tension/Sinistral	Few cm sinistral, 7 cm tension	VIII	VII	VII
100	24.0016	121.6141	Tension/Sinistral	Few cm sinistral, 2.5 cm tension	VIII	VII	VII
101	24.00102	121.6139	Compression	24 cm compression	VIII	VII	VII
102	24.001	121.614	Tension	16 cm tension	VIII	VII	VII
103	24.001	121.6139	Sinistral	15 cm sinistral offset	VIII	VII	VII
104	24.00055	121.6138	Tension/Sinistral	1–20 cm tension	VIII	VII	VII
105	24.00042	121.6137	Tension/Sinistral	1–20 cm tension	VIII-	VII	VII
106	24.0004	121.6138	Tension/Sinistral	1–20 cm tension	VIII	VII	VII
107	24.0003	121.6138	Tension/Sinistral	1–20 cm tension	VIII	VII	VII
108	24.00014	121.6137	Tension/Sinistral	1–20 cm tension	VIII	VII	VII
109	23.99998	121.6137	Tension/Sinistral	1–20 cm tension	VIII	VII	VII
110	23.9986	121.6134	Compression	20 cm tension	VIII	VII	VII
111	23.99826	121.6133	Sinistral	15 cm tension	VIII	VII	VII
112	23.99806	121.6134	Sinistral	Few cm sinistral offset	VIII	VII	VII
113	23.99582	121.6118	Tension	4 cm tension	VIII	VII	VII
114	23.99374	121.6125	Sinistral	10 cm sinistral offset	VIII	VII	VII
115	23.99127	121.6104	Compression	16 cm compression	VIII	VII	VII
116	23.98973	121.6096	Tension	3 cm vertical offset, 5 cm tension	VIII	VII	VII
117	23.98935	121.61	Sinistral/Reverse	4 cm sinistral offset, 5 cm vertical offset	VIII	VII	VII
118	23.98863	121.6098	Sinistral/Tension/ Subsidence	Few cm sinistral offset, 50 cm vertical offset, 35 cm tension	IX	VII	VII
119	23.98859	121.6093	Compression	5 cm vertical offset, 6 cm compression	VIII	VII	VII
120	23.98853	121.6096	Reverse	5 cm sinistral offset, 7 cm vertical, 12 cm compression	IX	VII	VII
121	23.98848	121.6096	Sinistral/Tension	5 cm sinistral offset, 16 cm tension	VIII	VII	VII
123	23.98716	121.6092	Sinistral/Reverse	500 cm long, 1 cm sinistral offset	IX	VII	VII
124	23.98694	121.6094	Dextral/Subsidence	25 cm Dextral offset	IX	VII	VII
125	23.98656	121.6095	Sinistral/Reverse	2 cm sinistral offset, 5 cm vertical offset	VIII	VII	VII
126	23.98656	121.6095	Sinistral/Reverse	200 cm long, 5 cm vertical offset	VIII	VII	VII
127	23.98625	121.6097	Compression	200 cm long, 30 cm compression	VIII	VII	VII
128	23.98622	121.6111	Sinistral/Reverse	2 cm sinistral offset with 1–10 cm vertical offset	VIII	VII	VII
129	23.9859	121.611	Sinistral	2 cm sinistral offset	VIII	VII	VII
130	23.98581	121.6101	Tension	200 cm long, 20 cm tension	VIII	VII	VII
131	23.98566	121.611	Sinistral/Tension	2 cm tension	VIII	VII	VII
132	23.98556	121.6111	Sinistral/Tension	1 cm sinistral offset 2 cm tension	VIII	VII	VII
133	23.98553	121.6102	Sinistral	4000 cm long 2 cm sinistral off set	IX	VII	VII
134	23.98488	121.6105	Tension	1.5 cm sinistral offset,3 cm tension	VIII	VII	VII
135	23.98379	121.609	Dextral	10 dextral offset	VIII	VII	VII
136	23.9892	121.6074	Tension	3 cm tension	VIII	VII	VII
137	23.98893	121.6074	Tension	5 cm tension	VIII	VII	VII
138	23.98888	121.6075	Tension	3 cm tension	VIII	VII	VII
139	23.98883	121.6075	Tension	5 cm tension	VIII	VII	VII
140	23.98881	121.6075	Tension	2 cm tension	VIII	VII	VII
141	23.98878	121.6075	Tension	3 cm tension	VIII	VII	VII
142	23.98865	121.6075	Tension	3 cm tension	VIII	VII	VII

(*continued on next page*)

Table 1 (*continued*)

Sl. No	Latitude	Longitude	Type of Displacement	Surface rupture dimensions (Length in cm, Horizontal offset and Vertical offset in cm)	Intensity		
					Esi-07	CWB	MM
143	23.98862	121.6075	Tension	2 cm tension	VIII	VII	VII
144	23.98859	121.6075	Tension	1.5 cm tension	VIII	VII	VII
145	23.98851	121.6076	Tension	1.5 cm tension	VIII	VII	VII
146	23.98768	121.608	Tension	6 vertical offset, 15 cm tension	VIII	VII	VII
147	23.98727	121.6082	Tension	2 cm vertical offset,2 cm tension	VIII	VII	VII
148	23.98726	121.6083	Tension	4 cm vertical offset,4 cm tension	VIII	VII	VII
149	23.98723	121.6077	Tension	2 cm vertical displacement,2 cm tension	VIII	VII	VII
150	23.98723	121.6082	Tension	2 cm vertical displacement, 2 cm tension	VIII	VII	VII
151	23.98722	121.6077	Tension	10 cm vertical displacement, 10 cm tension	VIII	VII	VII
152	23.98722	121.6083	Tension	6 cm vertical displacement, 6 cm tension	VIII	VII	VII
153	23.98721	121.6083	Tension	4 cm vertical displacement, 4 cm tension	VIII	VII	VII
154	23.98718	121.6083	Tension	3 cm vertical displacement,3 cm tension	VIII	VII	VII
155	23.98717	121.6082	Tension	5 cm vertical displacement,5 cm tension	VIII	VII	VII
156	23.98715	121.6083	Tension	1.5 cm vertical offset, 1.5 cm tension	VIII	VII	VII
157	23.98714	121.6077	Tension	5 cm vertical offset, 5 cm tension	VIII	VII	VII
158	23.98703	121.6084	Tension	2 cm vertical offset,2 cm tension	VIII	VII	VII
159	23.98703	121.6083	Tension	1.5 vertical offset,1.5 cm tension	VIII	VII	VII
160	23.98702	121.6083	Tension	2 vertical offset,2 cm tension	VIII	VII	VII
161	23.98701	121.6084	Tension	1 cm vertical offset,1 cm tension	VIII	VII	VII
162	23.987	121.6085	Tension	5 cm vertical offset,5 cm tension	VIII	VII	VII
164	23.98694	121.6085	Tension	3 cm vertical offset,3 cm tension	VIII	VII	VII
165	23.9869	121.6089	Tension	1.5 cm vertical offset,1.5 cm tension	VIII	VII	VII
166	23.980774	121.610275	Sinistral/Tension	Few cm sinistral offset with 5 cm tension	VIII	VII	VII
167	23.98065	121.61045	Sinistral/Tension	Few cm sinistral offset with 1 cm tension	VIII	VII	VII
168	23.98049	121.610329	Compression	Few cm sinistral offset with 20 cm compression	VIII	VII	VII
169	23.98049	121.610329	Sinistral	1 cm sinistral offset	VIII	VII	VII
170	23.979282	121.610336	Sinistral/Tension	10 cm sinistral offset with 5–10 cm tension	VIII	VII	VII
171	23.979164	121.610532	Sinistral/Tension	Few cm sinistral offset with 3 cm tension	VIII	VII	VII
172	23.978911	121.610724	Sinistral/Tension	2 cm sinistral offset with 3 cm tension	VIII	VII	VII
173	23.97827	121.61069	Dextral	1 cm dextral off set	VIII	VII	VII
174	23.978002	121.610308	Sinistral	5 cm sinistral offset	VIII	VII	VII
175	23.978002	121.610308	Tension	Few cm sinistral offset with 3–5 cm tension	VIII	VII	VII
176	23.977981	121.610182	Sinistral	1 cm sinistral offset	VIII	VII	VII
177	23.976664	121.611017	Sinistral/Tension	100 cm long sinistral offset	-IX	VII	VII
178	23.976664	121.611017	Sinistral/Tension	80 cm long sinistral offset	IX	VII	VII
179	23.97641	121.61069	Compression	3–5 cm compression	VIII	VII	VII
180	23.975745	121.609541	Sinistral	3 cm sinistral offset	VIII	VII	VII
181	23.975533	121.609167	Sinistral	2 cm sinistral offset	VIII	VII	VII
182	23.975371	121.60919	Sinistral/Tension	1 cm Sinistral offset, 3–5 cm tension	VIII	VII	VII
183	23.975486	121.609217	Sinistral	1 cm sinistral offset	VIII	VII	VII
184	23.974758	121.60972	Shear	1–2 sinistral offset	VIII	VII	VII
185	23.974782	121.609641	Sinistral	1~2 sinistral offset	VIII	VII	VII
186	23.974749	121.60956	Sinistral	1–2 sinistral offset	VIII	VII	VII
187	23.974686	121.609519	Dextral	3 cm dextral offset	VIII	VII	VII
188	23.974609	121.60948	Sinistral	3 cm sinistral offset	VIII	VII	VII
189	23.974522	121.609572	Sinistral	3 cm sinistral offset	VIII	VII	VII
190	23.974532	121.611098	Sinistral/Tension	1000 cm long, 2 cm sinistral offset, 1.5 cm tension	IX	VII	VII
191	23.974375	121.610819	Sinistral/Tension	1200 cm long, 3–4 cm sinistral offset,2 cm tension	IX	VII	VII
192	23.974352	121.610767	Sinistral/Tension	1000 cm long, 2 cm sinistral offset, 1 cm tension	IX	VII	VII
193	23.974275	121.610676	Sinistral/Tension	1000 cm long, 1 cm sinistral offset,1 cm tension	IX	VII	VII
194	23.973662	121.610929	Sinistral/Tension	800–1300 cm long and few cm sinistral offset	IX	VII	VII
195	23.973727	121.610901	Sinistral/Compression	100 cm long and few cm sinistral offset	VIII	VII	VII
196	23.973678	121.609642	Sinistral	1 cm sinistral offset	VIII	VII	VII
197	23.973913	121.609618	Sinistral	4 cm sinistral offset, 5 cm tension	VIII	VII	VII
198	23.973646	121.609367	Sinistral	Few cm sinistral offset, 8 cm compression,3 cm tension	VIII	VII	VII
199	23.973608	121.609305	Sinistral	Few cm sinistral offset,5 cm compression,2 cm tension	VIII	VII	VII
200	23.972069	121.609555	Sinistral/Tension	7000 cm long, few cm sinistral offset	IX	VII	VII
201	23.971975	121.609844	Sinistral/Tension	2 cm sinistral offset, 2 cm tension	VIII	VII	VII
202	23.97213	121.609766	Sinistral/Tension	2000–6000 cm long and few cm sinistral offset	IX	VII	VII
203	23.972051	121.609763	Sinistral/Compression	4000 cm long, few cm sinistral offset and 10 cm compression	IX	VII	VII
204	23.971574	121.609961	Tension	1300 cm long,15 cm vertical offset,10 cm tension	IX	VII	VII
205	23.971375	121.610034	Sinistral/Tension	1000 cm long,15 cm vertical offset,10 cm tension	IX	VII	VII
206	23.97125	121.610097	Tension	2800 cm long,15 cm vertical offset,15 cm tension	IX	VII	VII
207	23.970303	121.612805	Sinistral/Reverse	20 cm sinistral offset, 6 cm vertical offset, 8 cm compression	IX	VII	VII
208	23.970663	121.611755	Sinistral/Tension	3000 cm long and few cm sinistral offset,1.5 cm tension	IX	VII	VII
209	23.970755	121.611686	Sinistral/Tension	200 cm long, few cm sinistral offset, 0.5 cm tension	VIII	VII	VII
210	23.969188	121.61088	Sinistral/Tension	2 cm sinistral offset, 3 cm tension	VIII	VII	VII
211	23.968578	121.611276	Sinistral	5 cm sinistral offset	VIII	VII	VII
212	23.968425	121.611341	Sinistral	5 cm sinistral offset	VIII	VII	VII
213	23.968035	121.611678	Sinistral	2 cm sinistral offset	VIII	VII	VII
214	23.968055	121.610235	Sinistral	1 cm sinistral offset	VIII	VII	VII
215	23.9937	121.612	Sinistral	10 cm sinistral offset	VIII	VII	VII

Fig. 6. Typical field photos showing surface ruptures observed around the north Meilun. (a) 5 cm sinistral offset of polyurethane running tracks showing en echelon shear cracks at National Dong Hwa University, Meilun campus (NDHU). (b) Shear cracks showing 15 cm lateral displacement, push-up structures, and restraining bends observed at National Dong Hwa University (NDHU), Meilun campus. (c) One of the multiple offsets observed towards the south of the NDHU campus showed 20 cm sinistral offset during the February 6, 2018 Hualien earthquake (Photo credits: Huang et al., 2019).

earthquake produced a maximum 15 cm sinistral offset with S-shaped mole tracks. Towards the south, the surface rupture shows a series of NW striking en echelon tensional cracks, which are around 90 m long. Most cracks are 1–20 cm wide and more than 2 m long. The surface rupture further extends towards the southern tip of Mt. Meilun. Towards the western flank of Mt. Meilun, the surface rupture shows a series of restraining deformation structures (such as buckled and S-shaped mole tracks). The surface deformation observed along the northern bank of the Meilun River shows both dextral and sinistral push-up ridges (Table 1; Huang et al., 2019; Hsu et al., 2019).

Around downtown of Hualien, the rupture shows a very complex pattern. Near the Mingli elementary school, the rupture shows NW striking shear cracks and E-W striking push-up ridges (Table 1; Huang et al., 2019; Hsu et al., 2019). Through the school, the rupture extends to Hualien city, where the rupture does not restrict to a narrow width like the northern part of the rupture, such as Chihsingtan Beach or Mt. Meilun. In the city, the rupture is wider (~270 m wide) and shows ~10–15 cm sinistral offset.

Near the downtown night market, it shows extensive tensional cracks, several push-up ridges, and en-echelon fissures (Table 1; Huang et al., 2019; Hsu et al., 2019). Towards the south of the night market, the rupture entered the gravelly beach, where it was difficult to track (Huang et al., 2019; Hsu et al., 2019). The surface rupture extends to the northern segment of the Lingding fault, confirmed by field survey and interferogram analysis (CGS, 2018). The co-seismic deformation along the Lingding fault starts from the north side of the Hualien Bridge to the southwest and terminates at 1.7 km northeast of the Yuemei Bridge (Table 2). The total length of the rupture was about 6.2 km long, with an average strike of N33°E.

The surface deformation is almost entirely located on the sandbanks of the Hualien River. The surface expressions were modified by the river water and tidal activity, which was not an easy task for the researchers to map the surface rupture. The co-seismic surface deformation of the Lingding fault starts from the Hualien Bridge, which is about 180 m wide. The rupture here was divided into east, west, and central segments. The easternmost part extends with a strike N18°E for a length of 350 m passing through the Hualien Bridge. The central segment of the rupture was 880 m long, whereas the westernmost rupture was 380 m

Table 2
The details of surface rupture observed along the northern segment of Lingding fault (measurements are taken from CGS, 2018); MM intensity from were taken from USGS, last accessed January 10, 2022; CWB intensity values were taken from Central Weather Bureau, Seismological Division, Taiwan, last accessed January 10, 2022).

Sl. No	Latitude	Longitude	Type of Displacement	Surface rupture dimensions (Length, Horizontal offset (m) and Vertical offset in cm	Intensity		
					ESI	CWB	MM
1	23.9212	121.5991	Sinistral	**3m compression and 0.20 m uplift**	VIII	VII	**VII**
2	23.9229	121.5993	Sinistral	0.70 m sinistral offset	VIII	VII	VII
3	23.9218	121.5974	Sinistral	350 m long	IX	VII	VII
4	23.9240	121.5979	Sinistral	530 m long	IX	VII	VII
5	23.9219	121.5961	Sinistral	420 m long	IX	VII	VII
6	23.9077	121.5885	Sinistral	1500 m long	IX	VII	VI
7	23.9066	121.5876	Sinistral	1500–2000 m long, 50 m wide	IX	VII	VI
8	23.8997	121.5824	Sinistral	540 m long and 60 m wide	IX	VII	VI
9	23.8852	121.5709	Sinistral	400 m long and 25 m wide	IX	VII	VI

long. The rupture further extends towards SW to the Mugau River from the Hualien Bridge for a length of 1.5–2 km, where the rupture zone width is about 50 m. The rupture at this location shows en echelon ruptures with a strike of N45°–70°E. The rupture pattern observed here coincides with previously mapped fault traces. The rupture extends for a length of 540 m and a width of 60 m in the direction of S30°W from Mugau River. The rupture extends along the 193 County road 30 K with a strike of N45°-50°E for a length of 400 m and a width of 25 m. The surface rupture extends to the east end of the Yuemei Bridge, and afterward, it was challenging to trace the shreds of evidence of surface rupture. Therefore, the Yuemei Bridge has been considered the end point of the surface rupture along the northern Lingding fault.

Fig. 7. Field photographs showing observed cracks during February 6, 2018 Hualien earthquake. (a) Surface cracks observed along the south bank of Meilun River. (b) 10 cm wide and several meter-long surface cracks at the night market, Hualien city. (c) Several meter long and 8 cm wide tensional cracks at north of the Mingli elementary school. (d) Crack observed on road near the Marshal Hotel. (e) Cracks on the platform of the Hualien Railway Station. (f) Observed cracks at the Chihsingtan Bridge (Photo: Huang et al., 2019; Fischer et al., 2018; https://news.ltn.com.tw/news/life/breakingnews/233484; https://udn.com/news/story/6656/297361).

It should be remarked that the evidence described above and in Table 1 is only a partial illustration of the co-seismic surface rupture since the Milun fault offshore extension (Fig. 3b) has not been investigated.

4.2. Secondary effects

The secondary EEEs mostly concord with the ground shaking during an earthquake, including soil liquefaction, ground cracks, landslide/rock falls, and so on (Fig. 5). During the 2018 Hualien earthquake, several secondary effects such as liquefaction, sporadic small-scale rockfalls, slope failures along cliff sides and hillside highways, ground cracks along paved roads and grounds, and significant ground settlements due to soil liquefaction were reported. Several buildings, such as Beauty Stay Hotel, Marshal Hotel, and Yun Men Tsui Ti residential building in Hualien, were collapsed or tilted. The detailed analysis of the secondary effects is discussed in the following sections.

4.2.1. Ground cracks

Apart from the extensive surface rupture, ground cracks were the most common secondary earthquake environmental effects observed soon after the 2018 Hualien earthquake. Huang et al. (2019) detailed mapping of the surface ruptures and ground cracks, which were classified into three categories based on their location and tectonic significance. Category 1 was directly associated with the significant ruptures related to the slip surface, whereas Category 2 consists of surface deformation outside the central fault zone. Category 2 had a wider damage zone mainly composed of pressure ridges, mole tracks, and shear cracks with minor strike-slip movements. Cracks of Category 3 were not directly associated with fault movement; instead, it is directly related to ground shaking, local soil effects and ground engineering. Category 3 cracks include fissures/cracks on the ground, paved roads, etc. In this section, we have compiled all the Category 3 type cracks (Figs. 3b, 5 and 7; Table 3). Most of the ground cracks or cracks on the paved road were observed around the Huaxi road area, Hualien County, night market, Changan Street, and so on. The quantitative data for the ground cracks were used for the ESI-07 intensity estimation.

4.2.2. Liquefaction

During the February 6, 2018 earthquake, extensive liquefactions were observed around the epicentral area apart from the surface rupture. The liquefaction and ground settlement features were observed in the plain area of Hualien city (Hualien airport; Hualien railway station; Hualien county; Meilun River, Port of Hualien; Beibin, Nanbin Park, Jian, Soufeng area) (Ko et al., 2019) and Hualien River area along the Lingding fault (CGS, 2018, Table 4).

Most of the liquefied sites were reclaimed lands, paleo-channel sites composed of terrace deposits, flood plain deposits, and alluvium, making them liquefaction susceptible (Ko et al., 2019). It is well understood that the alluvial soils in saturated condition are susceptible to liquefaction during an earthquake. Due to subsequent rain, most of the sand boils could not give any quantitative information soon after the earthquake. Most of the post-earthquake survey reports or researches only reported the location of sand boils without the information on the diameters of the sand boils. However, the physical observations suggest that most of the sand boils were in the size of a few cm to 1 m in diameter (Fig. 8). At some locations, sand boils were observed (CGS, 2018), showing 75 m long and 45 m wide zone. Ko et al. (2019) reported that most of the sand boils around the Hualien airport had a diameter of no more than 1.5 cm sand vents.

During the earthquake, the areas to the south of Guosheng 8th street, north of Linsen road, and east of Guolian 5th road experienced slight subsidence, some sediments collapsed on the riverbank, and some ditches and fields show evidence of soil liquefaction. The ground in this area subsided about 5–8 cm (Ko et al., 2019). In the area between Shuimen and Guosheng 8th street, both the Meilun River's embankments collapsed, showing extensive liquefaction on both sides of the riverbed. (CGS, 2018). Minor lateral spreading/ground cracks were observed along the Meilun riverbanks, where the fractures were several meters long and 30–40 m wide (Ko et al., 2019).

Several liquefaction features were observed within the sandy beds of the Hualien river near the Hualien bridge, along with small-scale lateral spreading at the right bank of the Hualien River Estuary (CGS, 2018; Ko et al., 2019). The liquefaction features were several meters long and had a diameter of about a few cm to 1 m (CGS, 2018, Fig. 8).

Several wharves were damaged due to liquefaction-induced ground settlement at Port of Hualien. Wharves 19 showed a 10 cm of settlement, whereas wharf 23 showed a 20 cm of settlement. Similarly, wharf 24 shows a 25 cm of settlement, whereas wharf 25 shows a 40–60 cm settlement along with the occurrences of the sand boil. Several meters-long cracks were developed on the pavement along wharfs 23 and 24. The width of the cracks was about 10 cm (Ko et al., 2019).

4.2.3. Slope failure

The earthquake caused several small-scale ($\leq 10^3$–10^5 m^3) landslides/rock falls around Su-Hau Highway and Hualien Bridge. But there is no description of the geomorphology of the setting available in the published literature (e.g., slope dip; rock type). The rock falls near the Hualien Bridge blocked the main road with scattered rock fragments and trees. Most researchers focused on mapping the surface ruptures and associated features. Thus, less attention has been given to the estimation of the volume of the rock falls.

5. Intensity scales in Taiwan

Seismic intensity estimation in Taiwan solely relies on instrumental data (Wald et al., 1999; Wu et al., 2003). Seismic monitoring of Taiwan started a century ago (in the 1930s), and the earthquake intensity has been reported using an instrumental scale akin to the JMA intensity scale and MMI intensity scale. The seismic intensity scale in Taiwan is known as the CWB intensity scale and is based on the PGA intensity scale. Initially, it had seven intensity levels (I = 0–6) where each intensity corresponded to a specified PGA range (Wald et al., 1999; Wu et al., 2003; Ota et al., 2009). After the 1999 Chi-Chi earthquake, the addition of the intensity I = 7 was necessary to consider the severity of the shaking and damage induced by the earthquake due to widespread high PGA (>400 gal) (Table 5; Tsai et al., 2001; Wu et al., 2003). The CWB intensity was again revised in 2020 to a 10-degree intensity scale from January 2020, considering the 1370 earthquakes that occurred in Taiwan between 2009 and 2018. The new intensity scale shows the highest intensity value of I = 7, the same as the pre-2020 version of the CWB intensity scale. The maximum intensity level I = 7 was kept, as it is to protect the current laws and regulations related to earthquake hazards. The new CWB intensity scale considers PGV values in intensity estimation for seismic intensity higher than I = 5 as the intensity higher than this can cause structural damage. In the new intensity scale, the intensity values I = 5 and I = 6 were further subdivided into two other sub-values. According to the new intensity scale, Intensity 5-moderate quakes are characterized by difficulty walking and falling bricks from some structures. Intensity 5-strong can cause widespread panic and the collapse of weak brick walls.

Similarly, in Intensity 6-moderate, people have difficulty standing, weaker houses can collapse, cracks can appear on some roads, and landslides in mountainous areas, whereas, in Intensity 6-strong, stronger houses can be damaged. According to Wu et al. (2003), in terms of PGA, CWB intensity VI is equivalent to MM intensity VIII (Table 5). From the table, it can be inferred that the comparison of peak ground motion and intensities are based on the regressions of the intensity level against the recorded PGA values (Trifunac and Brady, 1975; Hsu, 1979; Wu et al., 2003). Some recent studies suggested that the intensity assessment using PGA or PGV is quite erratic due to the highly variable local site and wave propagation effects (Wu et al., 2003; Papanikolaou and Melaki, 2017;

Table 3
Detailed cracks observed around the Hualien city (measurements are taken from Huang et al., 2019; MM intensity from were taken from USGS, last accessed January 10, 2022; CWB intensity values were taken from Central Weather Bureau, Seismological Division, Taiwan, last accessed January 10, 2022).

Sl. No	Latitude	Longitude	Type of EEEs	Dimensions	Intensity		
					ESI	CWB	MM
1	23.981248	121.610016	Road damage	15 cm compression	VII	VII	VII
2	23.98189	121.6098	Road damage	Few cm sinistral off set	VII	VII	VII
3	23.982083	121.609964	Road Damage	Few cm wide compressional cracks	VII	VII	VII
4	23.982176	121.609963	Road damage	5 cm wide compressional cracks	VII	VII	VII
5	23.984304	121.609825	Road damage	Few cm tensional cracks	VII	VII	VII
6	23.98163	121.61845	Road damage	Few cm tensional cracks	VII	VII	VII
7	23.981506	121.601478	Road Damage	Few cm tensional cracks	VII	VII	VII
8	23.980712	121.599637	Road damage	0.5 cm tensional cracks	VII	VII	VII
9	23.980443	121.595612	Road damage	Few cm tensional cracks	VII	VII	VII
10	23.980119	121.596776	Road damage	Few cm tensional cracks	VII	VII	VII
11	23.979877	121.597997	Road damage	2 cm wide tensional cracks	VII	VII	VII
12	23.979704	121.601803	Road damage	1 cm wide compressional cracks	VII	VII	VII
13	23.97965	121.601051	Road damage	2 cm wide tensional cracks	VII	VII	VII
14	23.979642	121.600108	Road damage	Few cm tensional cracks	VII	VII	VII
15	23.979498	121.599371	Road damage	0.5 cm tensional cracks	VII	VII	VII
16	23.979342	121.597737	Road damage	1 cm tensional cracks	VII	VII	VII
17	23.979003	121.600431	Road damage	1 cm tensional cracks	VII	VII	VII
18	23.978656	121.600204	Road damage	1 cm tensional cracks	VII	VII	VII
19	23.978209	121.597937	Road damage	0.5 cm tensional cracks	VII	VII	VII
20	23.977674	121.598011	Road damage	1 cm tensional cracks	VII	VII	VII
21	23.977594	121.59811	Road damage	1 cm tensional cracks	VII	VII	VII
22	23.97738	121.598397	Road damage	Few cm tensional cracks	VII	VII	VII
23	23.982897	121.608048	Road damage	Few cm compressional cracks	VII	VII	VII
24	23.982806	121.608092	Road damage	Few cm compressional cracks	VII	VII	VII
25	23.982766	121.60812	Road damage	Few cm compressional cracks	VII	VII	VII
26	23.981724	121.608967	Road damage	2 cm compressional cracks	VII	VII	VII
27	23.981547	121.609089	Road damage	5 cm compressional cracks	VII	VII	VII
28	23.980811	121.608686	Road Damage	4 cm compressional cracks	VII	VII	VII
29	23.98065	121.61045	Road damage	1 cm tensional cracks	VII	VII	VII
30	23.98049	121.610329	Infrastructure damage	20 cm compressional cracks	VII	VII	VII
31	23.98049	121.610329	Road damage	1 cm sinistral cracks	VII	VII	VII
32	23.98002	121.610268	Road damage	Few cm Sinistral/Compression cracks	VII	VII	VII
33	23.979881	121.610391	Road damage	Few cm Sinistral cracks	VII	VII	VII
34	23.98018	121.61159	Infrastructure damage	4 cm tensional cracks	VII	VII	VII
35	23.97974	121.61028	Road damage	1 cm tensional cracks	VII	VII	VII
36	23.979641	121.610381	Road damage	1 cm tensional cracks	VII	VII	VII
37	23.979282	121.610336	Road damage	5–10 cm tensional cracks	VII	VII	VII
38	23.979164	121.610532	Infrastructure damage	3 cm tensional cracks	VII	VII	VII
39	23.978911	121.610724	Infrastructure damage	3 cm tensional cracks	VII	VII	VII
40	23.978649	121.61087	Road damage	0.5 cm tensional cracks	VII	VII	VII
41	23.978649	121.61087	Road damage	0.5 cm tensional cracks	VII	VII	VII
42	23.978381	121.610905	Road damage	0.5 cm tensional cracks	VII	VII	VII
43	23.978381	121.610905	Road damage	0.5 cm tensional cracks	VII	VII	VII
44	23.978002	121.610308	Road damage	3–5 cm tensional cracks	VII	VII	VII
45	23.977875	121.610132	Road damage	1 cm tensional cracks	VII	VII	VII
46	23.977875	121.610132	Road damage	1 cm tensional cracks	VII	VII	VII
47	23.976799	121.61002	Road damage	0.1 cm tensional cracks	VII	VII	VII
48	23.976913	121.60996	Road damage	0.1 cm tensional cracks	VII	VII	VII
49	23.977077	121.609801	Road damage	0.1 cm tensional cracks	VII	VII	VII
50	23.977128	121.60973	Road damage	1 cm tensional cracks	VII	VII	VII
51	23.977128	121.60973	Road damage	1 cm tensional cracks	VII	VII	VII
52	23.977421	121.609408	Road damage	2 cm tensional cracks	VII	VII	VII
53	23.97681	121.610479	Road damage	10 cm compressional cracks	VII	VII	VII
54	23.976664	121.611017	Road damage	100 cm long cracks	VIII	VII	VII
55	23.976664	121.611017	Road damage	80 cm cracks	VIII	VII	VII
56	23.97641	121.61069	Infrastructure damage	3–5 cm compressional cracks	VIII	VII	VII
57	23.976147	121.610951	Road damage	1 cm tensional cracks	VIII	VII	VII
58	23.976147	121.610951	Road damage	1 cm tensional cracks	VIII	VII	VII
59	23.976147	121.610951	Road damage	0.5 cm tensional cracks	VIII	VII	VII
60	23.97596	121.61149	Road damage	0.5 cm tensional cracks	VIII	VII	VII
61	23.97573	121.61049	Infrastructure damage	6 cm compressional cracks	VIII	VII	VII
62	23.974913	121.609903	Road damage	32 cm compressional cracks	VIII	VII	VII
63	23.975533	121.609167	Road damage	2 cm sinistral cracks	VIII	VII	VII
64	23.975371	121.60919	Road damage	3 cm tensional cracks	VIII	VII	VII
65	23.975406	121.609253	Road damage	3 cm tensional cracks	VIII	VII	VII
66	23.975486	121.609217	Road damage	1 cm sinistral offset	VIII	VII	VII
67	23.970785	121.610333	Road damage	8 cm compressional cracks	VIII	VII	VII
68	23.970275	121.61062	Road damage	14 cm compressional cracks	VIII	VII	VII
69	23.970188	121.610673	Road damage	16 cm compressional cracks	VIII	VII	VII
70	23.971388	121.611189	Road damage	Few cm Uplift/Subsidence	VIII	VII	VII
71	23.971605	121.610887	Road damage	Few cm Uplift/Subsidence	VIII	VII	VII
72	23.972021	121.610567	Road damage	Few cm Uplift/Subsidence	VIII	VII	VII

(*continued on next page*)

Table 3 (*continued*)

Sl. No	Latitude	Longitude	Type of EEEs	Dimensions	Intensity		
					ESI	CWB	MM
73	23.969459	121.610764	Road Damage	6 cm vertical uplift	VIII	VII	VII
74	23.969696	121.612046	Road Damage	3 cm vertical uplift	VIII	VII	VII
75	23.969188	121.61088	Infrastructure damage	3 cm tensional cracks	VIII	VII	VII
76	23.969053	121.610973	Infrastructure damage	5 cm tensional cracks	VIII	VII	VII
77	23.968804	121.611188	Infrastructure damage	Collapse of buildings	VIII	VII	VII
78	23.968117	121.611731	Road Damage	9 cm tensional cracks	VIII	VII	VII
79	23.97195	121.61386	Road damage	2 cm compressional cracks	VIII	VII	VII
80	23.968656	121.610059	Road damage	1 cm tensional cracks	VIII	VII	VII
81	23.967739	121.61146	Road damage	3.5 cm tensional cracks	VIII	VII	VII
82	23.966721	121.610683	Road damage	4 cm tensional cracks	VIII	VII	VII
83	23.965771	121.609973	Road damage	3 cm tensional cracks	VIII	VII	VII
84	23.965533	121.609787	Road damage	2 cm sinistral and 3 cm tensional cracks	VIII	VII	VII
85	23.964887	121.609309	Road damage	2 cm tensional cracks	VIII	VII	VII
86	23.9633	121.60806	Road damage	2 cm tensional cracks	VIII	VII	VII
87	23.96326	121.60763	Road damage	5 cm compressional cracks	VIII	VII	VII
88	23.96227	121.60759	Road damage	1 cm tensional cracks	VIII	VII	VII
89	23.96291	121.60635	Road damage	2 cm tensional cracks	VIII	VII	VII
90	23.94661	121.60354	Road damage	5 cm compressional cracks	VIII	VII	VII
91	23.966296	121.608449	Road damage	0.5 cm tensional cracks	VIII	VII	VII
92	23.9716667	121.6003944	Road damage	3 cm compressional cracks	VIII	VII	VII
93	23.9696472	121.5987389	Road damage	1.5 cm compressional cracks	VIII	VII	VII
94	23.9682	121.5994639	Road damage	0.3 cm tensional cracks	VIII	VII	VII
95	23.96411	121.60717	Infrastructure damage	4 cm tensional cracks	VIII	VII	VII
96	24.00259	121.6129	Road damage	1 cm tensional cracks	VIII	VII	VII
97	24.0016	121.6141	Road damage	2 cm tensional cracks	VIII	VII	VII
98	24.0016	121.6141	Road damage	9 cm tensional cracks	VIII	VII	VII
99	24.0016	121.6141	Road damage	12 cm tensional cracks	VIII	VII	VII
100	24.0016	121.6141	Road damage	1.5 cm tensional cracks	VIII	VII	VII
101	24.0016	121.6141	Road damage	7 cm tensional cracks	VIII	VII	VII
102	24.0016	121.6141	Road damage	2.5 cm tensional cracks	VIII	VII	VII
103	24.00102	121.6139	Road damage	24 cm compressional cracks	VIII	VII	VII
104	24.001	121.614	Road damage	16 cm compressional cracks	VIII	VII	VII
105	23.99958	121.6232	Road damage	1.5 cm tensional cracks	VIII	VII	VII
106	23.99582	121.6118	Road damage	4 cm tension	VIII	VII	VII
107	23.99524	121.6083	Road damage	4 cm tension	VIII	VII	VII
108	23.99498	121.608	Road damage	4 cm tension	VIII	VII	VII
109	23.9943	121.6107	Road damage	1 cm tension	VIII	VII	VII
110	23.99428	121.6115	Road damage	3 cm tension	VIII	VII	VII
111	23.99382	121.6092	Road damage	10 cm tension	VIII	VII	VII
112	23.99266	121.6085	Road damage	3.5 cm compression	VIII	VII	VII
113	23.99239	121.6126	Road damage	1 cm Tension	VIII	VII	VII
114	23.99187	121.6093	Bridge damage	25 cm horizontal offset	VIII	VII	VII
115	23.99171	121.6111	Road damage	1 cm tension	VIII	VII	VII
116	23.99169	121.6126	Road damage	2 cm tension	VIII	VII	VII
117	23.99147	121.6111	Road damage	1 cm tension	VIII	VII	VII
118	23.99137	121.6067	Road damage	1 cm tension	VIII	VII	VII
119	23.99127	121.6104	Road damage	16 cm compression	VIII	VII	VII
120	23.98887	121.6001	Road damage	2 cm tension	VIII	VII	VII
121	23.98859	121.6093	Infrastructure damage	5 cm vertical displacement with 6 cm compression	VIII	VII	VII
122	23.98807	121.6062	Road damage	5 cm compression	VIII	VII	VII
123	23.98635	121.6097	Infrastructure damage	5 cm compression	VIII	VII	VII
124	23.98625	121.6097	Infrastructure damage	30 cm compression	VIII	VII	VII
125	23.98581	121.6101	Infrastructure damage	200 m long and 20 cm extensional cracks	VIII	VII	VII
126	23.98566	121.611	Infrastructure damage	2 cm extensional cracks	VIII	VII	VII
127	23.98487	121.6188	Road damage	1 cm extensional cracks	VIII	VII	VII
128	23.98446	121.6111	Road damage	8–10 cm compressional cracks	VIII	VII	VII
129	23.98716	121.6078	Road damage	6 cm compression	VIII	VII	VII
130	23.98684	121.6079	Road damage	4 cm compression	VIII	VII	VII
131	23.98627	121.6083	Road damage	13 cm compression	VIII	VII	VII
132	23.98623	121.6087	Road damage	21 cm compression	VIII	VII	VII
133	24.021888	121.62636	Road damage	5 cm compression	VIII	VII	VII
134	24.021465	121.626185	Road damage	10 cm compression	VIII	VII	VII
135	24.021455	121.626175	Road damage	50 cm compression	VIII	VII	VII
136	24.021383	121.625869	Road damage	5 cm compression	VIII	VII	VII
137	24.013272	121.619098	Infrastructure damage	3 cm vertical uplift	VIII	VII	VII
138	24.013264	121.619086	Infrastructure damage	5 cm compression	VIII	VII	VII
139	24.011993	121.619149	Road damage	5 cm tension	VIII	VII	VII
140	24.011808	121.61893	Infrastructure damage	15 cm tensional cracks	VIII	VII	VII
141	24.011713	121.618885	Infrastructure damage	10 cm tensional cracks	VIII	VII	VII
142	24.010671	121.617843	Road damage	5 cm tensional cracks	VIII	VII	VII
143	24.0106	121.617807	Infrastructure damage	22 cm tensional cracks	VIII	VII	VII
144	24.010475	121.617702	Infrastructure damage	10 cm tensional cracks	VIII	VII	VII
145	24.01855	121.6296	Road damage	5 cm tensional cracks	VIII	VII	VII
146	24.01825	121.63548	Road damage	1 cm tensional cracks	VIII	VII	VII

(*continued on next page*)

Table 3 (*continued*)

Sl. No	Latitude	Longitude	Type of EEEs	Dimensions	Intensity		
					ESI	CWB	MM
147	24.013266	121.620428	Road damage	5 cm tensional cracks	VIII	VII	VII
148	24.012656	121.619851	Road damage	5 cm tensional cracks	VIII	VII	VII
149	24.011537	121.618905	Road damage	5 cm tensional cracks	VIII	VII	VII
150	24.0114852	121.6200088	Infrastructure damage	3 cm tensional cracks	VIII	VII	VII
151	24.0112575	121.6197743	Road damage	2.5 cm vertical t with 1 cm wide cracks	VIII	VII	VII
152	24.010454	121.617747	Road damage	18 cm tension	VIII	VII	VII
153	24.010454	121.617747	Road damage	6 cm tension	VIII	VII	VII
154	24.010454	121.617747	Road damage	10 cm tension	VIII	VII	VII
155	24.010384	121.618291	Road damage	3 cm tension	VIII	VII	VII
156	24.010384	121.618291	Road damage	3 cm tension	VIII	VII	VII
157	24.010327	121.618074	Road damage	5 cm tension	VIII	VII	VII
158	24.010117	121.61762	Road damage	25 cm tension	VIII	VII	VII
159	24.010081	121.618155	Road damage	5 cm tension	VIII	VII	VII
160	24.009192	121.617244	Infrastructure damage	20 cm tension	VIII	VII	VII
161	24.009061	121.617348	Infrastructure damage	10 cm compression	VIII	VII	VII
162	24.006637	121.615735	Infrastructure damage	4 cm compression	VIII	VII	VII
163	24.003325	121.614714	Road damage	3 cm tension	VIII	VII	VII
164	24.025337	121.629687	Bridge damage	30 cm tension	VIII	VII	VII
165	24.025517	121.629677	Bridge damage	10 cm tension	VIII	VII	VII
166	24.025517	121.629677	Bridge damage	10 cm tension	VIII	VII	VII
167	24.025836	121.630019	Road damage	3 cm tension	VIII	VII	VII
168	24.025788	121.630003	Road damage	3 cm tension	VIII	VII	VII
169	24.026244	121.630633	Infrastructure damage	40 cm tension	VIII	VII	VII
170	24.026165	121.630815	Infrastructure damage	5 cm tension	VIII	VII	VII
171	24.02662	121.631104	Infrastructure damage	73 cm compression	VIII	VII	VII
172	24.026772	121.632072	Road damage	40 cm compression	VIII	VII	VII
173	24.014564	121.619973	Uplift	30 cm uplift	VIII	VII	VII

Table 4

The location of liquefaction features and its dimensions observed during the 2018 Hualien earthquake (measurements are taken from Huang et al., 2019; Ko et al., 2019; CGS, 2018); MM intensity from were taken from USGS, last accessed January 10, 2022; CWB intensity values were taken from Central Weather Bureau, Seismological Division, Taiwan, last accessed January 10, 2022).

Sl. No	Latitude	Longitude	Type of EEEs	Liquefaction Dimensions	ESI Intensity	CWB Intensity	MM Intensity
1	24.01617	121.621487	Liquefaction	Few cm to around 1 m diameter	VIII	VII	VII
2	24.015807	121.620598	Liquefaction	Few cm to around 1 m diameter	VIII	VII	VII
3	24.015599	121.620308	Liquefaction	Few cm to around 1 m diameter	VIII	VII	VII
4	24.015575	121.621052	Liquefaction	Few cm to around 1 m diameter	VIII	VII	VII
5	24.015386	121.620857	Liquefaction	75 m length by 45 m wide zone with sand boils diameter more than 1 m	VIII	VII	VII
6	24.015292	121.620733	Liquefaction	Few cm to around 1 m diameter	VIII	VII	VII
7	24.015172	121.620592	Liquefaction	Few cm to around 1 m diameter	VIII	VII	VII
8	24.015063	121.620742	Liquefaction	Few cm to around 1 m diameter	VIII	VII	VII
9	24.015045	121.620481	Liquefaction	Few cm to around 1 m diameter	VIII	VII	VII
10	24.014539	121.619172	Liquefaction	Few cm to around 1 m diameter	VIII	VII	VII
11	24.014148	121.619387	Liquefaction	Few cm to around 1 m diameter	VIII	VII	VII
12	24.01408	121.619059	Liquefaction	Few cm to around 1 m diameter	VIII	VII	VII
13	24.014029	121.619159	Liquefaction	Few cm to around 1 m diameter	VIII	VII	VII
14	24.013976	121.619331	Liquefaction	Few cm to around 1 m diameter	VIII	VII	VII
15	24.013954	121.618681	Liquefaction	Few cm to around 1 m diameter	VIII	VII	VII
16	24.013821	121.618898	Liquefaction	Few cm to around 1 m diameter	VIII	VII	VII
17	24.013769	121.618887	Liquefaction	Few cm to around 1 m diameter	VIII	VII	VII
18	24.013555	121.619105	Liquefaction	Few cm to around 1 m diameter	VIII	VII	VII
19	23.98668	121.6088	Liquefaction	Few cm to around 1 m diameter	VIII	VII	VII
20	23.98556	121.6094	Liquefaction	Few cm to around 1 m diameter	VIII	VII	VII
21	23.981367	121.610037	Liquefaction	Few cm to around 1 m diameter	VIII	VII	VII
22	23.981423	121.609946	Liquefaction	Few cm to around 1 m diameter	VIII	VII	VII
23	23.982297	121.610099	Liquefaction	Few cm to around 1 m diameter	VIII	VII	VII
24	23.984152	121.61018	Liquefaction	Few cm to around 1 m diameter	VIII	VII	VII
25	23.984152	121.61018	Liquefaction	Few cm to around 1 m diameter	VIII	VII	VII
26	23.97747	121.62617	Liquefaction/ subsidence	30–50 cm vertical and 10 cm wide	VIII	VII	VII
27	23.97565	121.62655	Liquefaction	10 cm wide	VIII	VII	VII
28	23.97536	121.62517	Liquefaction	30–50 cm vertical and 10 cm wide	VIII	VII	VII
29	23.97289	121.61008	Liquefaction	Few cm to around 1 m diameter	VIII	VII	VII
30	23.972397	121.610521	Liquefaction	Few cm to around 1 m diameter	VIII	VII	VII
31	23.972215	121.610647	Liquefaction	Few cm to around 1 m diameter	VIII	VII	VII

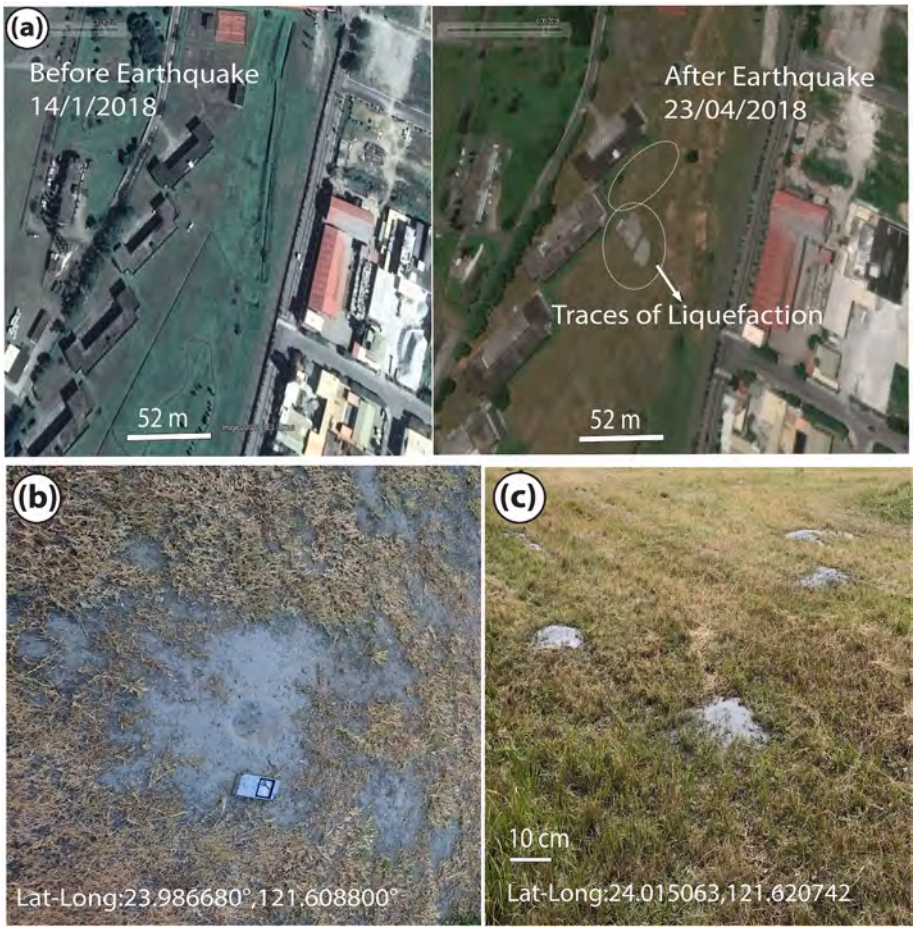

Fig. 8. (a) Pre- and post-earthquake Google Earth images showing evidences of liquefaction near the Hualien Airport. Liquefaction was observed in the post-earthquake satellite image (Image source: https://earthengine.google.com). (b) Field photograph showing the scattered liquefaction of a few cm to 1 m diameter for an area of 400 m *100 m near the Hualien airport. (c) Sand boils observed near the downtown of Hualien city during February 6, 2018 Hualien earthquake (Photo credit: Huang et al., 2019).

Table 5
CWB intensity scale and its comparison to MM Intensity scale (MM Intensity).

CWB Intensities (before 2020)	0	1	2	3	4	5		6		7	–
PGA (Gal	<0.80	0.8–2.5	2.5–8	8–25	25–80	80–250		250–400		>400	–
PGV (Cm/sec)	<0.22	0.22–0.65	0.65–1.9	1.9–5.7	5.7–17	17–49		49–75		>75	–
CWB Intensities (after 2020 modification)	0	1	2	3	4	5	5	6	6	7	–
PGA (Gal	<0.80	0.8–2.5	2.5–8	8–25	25–80	80–140	140–250	250–440	440–800	>800	–
PGV (Cm/sec)	<0.22	0.22–0.65	0.65–1.9	1.9–5.7	5.7–15	15–30	30–50	50–80	80–140	>140	
MM Intensities	**1**	**2–3**	**4**	**5**	**6**	**7**		**8**		**9**	**10**
PGA (Gal	<1.7	1.7–14	14–39	39–92	92–180	180–340		340–650		650–1240	>1240
PGV (Cm/sec)	<0.1	0.1–1.1	1.1–3.4	3.4–8.1	8.1–16	16–31		31–60		60–116	>116

Naik et al., 2020a). This was evident during Tarzana, 1994 Northridge earthquake, the USA, and the 2008 Wenchuan earthquake (Wu et al., 2003; Liu-Zeng et al., 2017). Wu et al. (2003) reported that, during large magnitude earthquakes, PGA/PGV values could vary depending on the sites and earthquake behavior in Taiwan. A similar observation was also made in Taiwan during the 2016 Meinong (M_w-6.4) and 2018 Hualien (M_w 6.4) earthquakes (Wu et al., 2016, 2019). Despite the same magnitude, both earthquakes caused buildings to collapse at different PGV values. During the 2018 Hualien earthquake, a 12-story building in the area that experienced high PGV (>49 m/s) was tilted. During the 2016 Meinong earthquake, buildings collapsed in areas with PGV values of around 17 m/s. This indicates that the structural damage pattern mainly depends on the local site effects. Noted that it will provide an erratically seismic intensity when intensity is determined considering the PGA/PGV values and the observed damage pattern associated with those PGA/PGV values. This was evident during the 2018 Hualien (M_w 6.4) earthquake. The CWB shows PGA values of less than 0.08 g measured by seismic stations, whereas the PGA values taken from P-alert instruments show PGA values of 0.008g–0.025 g (Wu et al., 2019). This indicates that the traditional intensity scale, which relies on structural parameters and variation of PGA and PGV, may over-predict or under-predict the seismic intensity (Papanikolaou, 2011). Also, the constant revision of the CWB intensity scale from six to seven and then to a ten-degree intensity scale within the last few decades demonstrate the inadequacy of the current CWB intensity scale. Papanikolaou (2011) argued that the use of many intensity scales worldwide (e.g., MM, MCS, MSK, JMA), which are also constantly updated (e.g., EMS, 1992; EMS, 1998; etc.), indirectly demonstrates the inefficiency of the current traditional intensity scales in describing the macroseismic earthquake effects and intensity. This problem can be overcome by the ESI-07 scale, which provides more accurate intensity due to its quantitative nature and its consideration of the geology, geotechnical, and morphological condition of the site when the intensity is determined. The ShakeMaps generated from the PGV and EEEs were compared in the present study.

5.1. ShakeMaps from EEEs

ShakeMaps (USGS Earthquake Hazards Program) are generally used for the earthquake early warning system to identify the strongly affected areas during an earthquake and to define the post-earthquake emergency plan for the affected areas. In such cases, the ShakeMaps are automatically generated and are not validated by initial human supervision, considering the urgency of rapid response survey and recovery. ShakeMaps can be developed for historical earthquakes or future seismic events, considering the local geology and ground effects caused by the historical earthquakes. ShakeMap generated by USGS Earthquake Hazards Program is available for modern seismic events worldwide, but existing ShakeMap related to historical earthquakes is rare (Silva et al., 2017). However, the ShakeMap generated by USGS Earthquake Hazards Program does not include the surface rupture or fault parameter data (Wald et al., 1999, 2005).

Like the USGS Earthquake Hazards Program, Central Weather Board (CWB), Taiwan also generates the ShakeMap for damaging earthquakes. The ShakeMap program used in Taiwan considers the instrumentally recorded PGA and PGV values (Yang et al., 2018; Wu et al., 2019; Mittal et al., 2019). However, it does not include the local geology for all the earthquakes due to the unavailability of the quantitative site descriptions, Vs30, the average shear-wave velocity over the top 30 m, for the all strong-motion sites of CWB (Liu et al., 2013). Recently, two earthquakes having similar magnitudes around Hualien city magnitude in 2018 (M_w 6.4) and 2019 (M_w 6.1) have produced different damage scenarios despite having the same ShakeMap (Yang et al., 2021; Mittal et al., 2021). This emphasizes the uncertainty of the current PGA ShakeMap/Intensity ShakeMap in Taiwan and the addition of geological ground effects with the instrumental data for a better ShakeMap generation. Silva et al. (2017) suggested that the detailed field mapping and documentation of the co-seismic environmental effects (EEE) can be used to prepare ShakeMaps for the historical and recent earthquakes. However, the model presented by Silva et al. (2017) for the generation of ESI-07 ShakeMaps follows the basic methodology similar to the USGS Shake Map program, which does not consider the surface rupture, which may underestimate the seismic hazard scenario.

Considering the uncertainty and demerits of the USGS Shake Map program and CWB intensity maps, we have tried to add the surface rupture data and co-seismic environmental effects (EEEs) for recent earthquakes in the ShakeMap for the 2018 Hualien earthquake. For generating the ShakeMap, we have used the Earthworm module, which is already an established method to prepare the ShakeMaps for earthquakes in Taiwan, considering the instrumentally recorded PGA and PGV values (Yang et al., 2018; Wu et al., 2019; Mittal et al., 2019). But this is a 1st ever attempt in Taiwan to generate the ShakeMap using the surface rupture data using the Earthworm program.

The Earthwork program receives the intensity value information from the input file and saves the values of each place. With these stored values, the Earthworm module will perform the spatial interpolation calculation using inverse distance weighting (Mittal et al., 2019; Wu et al., 2019; Yang et al., 2018; Legendre et al., 2017) to obtain a reasonable regional ShakeMaps. The Earthworm software has no graphical interface to represent the results in graphical form. So the GMT tool was used for drawing and publishing the image file of regional intensity ShakeMaps according to the data generated by the previous program.

6. Macroseismic intensity estimation using ESI-07

During the 2018 Hualien earthquake, both primary and secondary EEEs were extensively observed around the Hualien city and Lingding, which included surface rupture, liquefaction, slope failure, and ground cracks (Lin et al., 2019; Kuo et al., 2019; Hsu et al., 2019; Huang et al., 2019). The earthquake generated a ~7.5 km long trace of surface rupture along the Milun fault and a 6.2 km long rupture along the northern end of the Lingding fault (CGS, 2018; Huang et al., 2019; Lin et al., 2019; Hsu et al., 2019, Figs. 3 and 5).

Considering the primary and secondary environmental effects, we have prepared an ESI-07 intensity map based on the ESI-2007 guideline proposed by Michetti et al. (2007). Taking into account the observed and reported EEEs data, the ESI-07 and MM intensity for each reported location was assigned, and a spatial distribution map for the intensity was prepared (Tables 1–4; Fig. 9, Fig. S2). The ESI-07 intensity derived from the EEEs was compared with the CWB intensity and MM intensity scale (Fig. 5, Tables 1–4). Since the area is continuously affected by historical earthquakes, an attempt has been made to compare the ESI-07 intensity of historical earthquakes with the most recent earthquake (i.e., the 2018 Hualien earthquake). The macroseismic intensities of the 2018 Hualien earthquake were compared with the historical 1951 Hualien earthquake sequence. It was decided to apply the ESI-07 scale to this specific historical earthquake, like the 1951 Hualien earthquakes. The 2018 Hualien earthquakes are comparable in size, and types of primary and secondary effects, as well, as they share a commonly affected area. Except for the 1951 Hualien earthquake, the information on earthquake-induced ground effects of other historical earthquakes is scanty. Comparing the macroseismic intensity for those earthquakes with the 2018 Hualien earthquakes may underscore or overestimate the seismic intensity, hence the seismic hazard.

6.1. Macroseismic intensity estimation for 1951 Hualien earthquake

The study area has century-long historical seismicity records. Several damaging earthquakes, such as the events of 1920, 1951, and 1986. However, the EEEs are not well documented for the 1920 and 1986 Hualien earthquakes, whereas the EEEs for the 1951 earthquakes were reported by several researchers (Hsu, 1962; Shyu et al., 2007; Lee et al., 2008).

Plenty of documents supported by photographs have been used for the EEEs caused by the earthquake. Still, there are no available quantitative data to consider for a detailed macroseismic intensity for the earthquake (Shyu et al., 2007). Lee et al. (2008) estimated the surface rupture data from GPS measurements, showing the horizontal displacement varying from 4 m to less than 1 m (Table S1). Hsu (1962) reported the maximum horizontal offset observed from field measurements is about 2 m. Shyu et al. (2007) suggested that during the 1951 Hualien earthquake, ~70 km long surface rupture and liquefaction, ground cracks, and ground uplift were observed around the epicentral area. In addition, the 1951 Hualien earthquake caused a 2 m sinistral offset and 1.2 m vertical uplift along the Milun fault (Taiwan Weather Bureau, 1952; Hsu, 1962; Shyu et al., 2007; Lee et al., 2008), which was also ruptured during the 2018 Hualien earthquake. Although the total rupture was ~70 km long, we have taken the rupture length observed along the Milun fault, considering the same area affected by both the 1951 and 2018 earthquakes, to make a fair comparison of the ESI-07 scale between the historical and recent seismicity. Taking into account the reported length of the surface rupture (~9–10 km) and maximum displacement observed (2 m) along the Milun Fault, the epicentral intensity (I_0) was calculated (Taiwan Weather Bureau, 1952; Shyu et al., 2007) using the empirical relationship between epicentral intensity and faulting parameters proposed by Michetti et al. (2004).

$$I_0 = \mathrm{INT}\,[0.5503 \times L_n\,(\text{Surface Rupture Length}) + 7.861] \quad (1)$$

$$I_0 = \mathrm{INT}\,[0.5786 \times L_n\,(\text{Maximum Displacement}) + 9.51] \quad (2)$$

The estimated epicentral intensity for the 1951 Hualien earthquake is I_0 = X. The estimated intensity is the minimum value because the offshore faulting parameters have not been included in the rupture length due to a lack of observations and reports.

The CWB intensity distribution map (Taiwan Weather Bureau, 1952; Cheng et al., 1996) shows the maximum intensity of I═VI (Fig. S1; Table S1), whereas the MM intensity distribution map (MM data source:

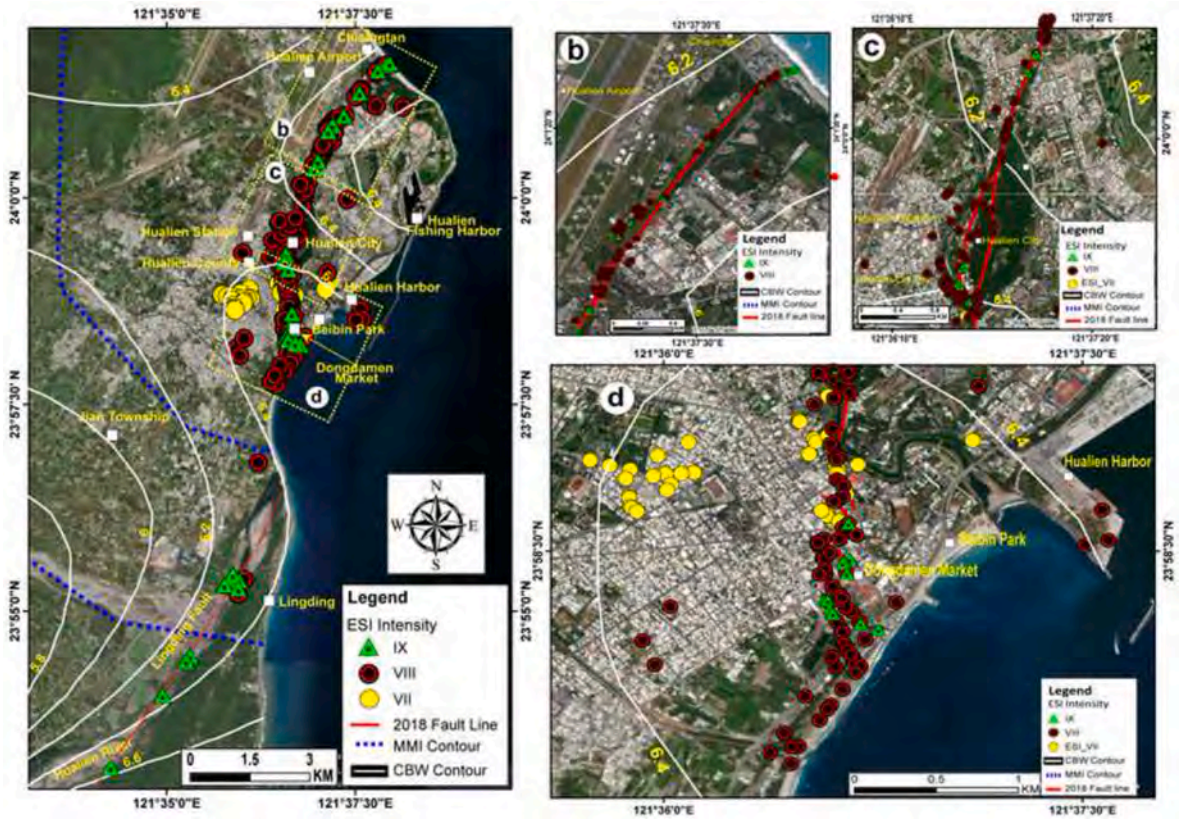

Fig. 9. (a) The ESI-07 intensity distribution for the 2018 Hualien earthquake based on the observed EEEs. Different color indicates the different ESI intensity, which varies from VII to IX. The white dotted line indicates the CWB intensity contours whereas the blue dotted line indicate the MMI contour. The yellow box (b, c, d) is showing the zoomed view of the ESI-07 intensity plot from different parts along the Milun fault trace (Image source: Image source: Esri, Digital Globe, Geo Eye, i-cubed, USDA FSA, USGS, AEX, Get mapping, Aero grid, IGN, IGP, Swiss topo, and the GIS User Community. (For interpretation of the references to color in this figure legend, the reader is referred to the Web version of this article.)

https://earthquake.usgs.gov/earthquakes/eventpage/iscgem894828/map) shows the intensity of I=VII for the 1951 Hualien earthquake. However, the estimated ESI-07 intensity shows 1–4 degrees' higher intensity for the earthquake than the traditional CWB and MM intensity scales.

6.2. Macroseismic intensity estimation for 2018 Hualien earthquake

Around 450 observed and reported data sets of both primary and secondary EEEs during the 2018 Hualien earthquake were used to assess the macroseismic intensity for the epicentral zone of the earthquake. The post-earthquake survey showed that most of the liquefaction features were observed along paleo lakes and river beds and present-day river beds. In contrast, the surface ruptures were concentrated along the pre-identified Lingding and Milun faults. The localized landslides were observed along the hilly terrains. In contrast, the ground cracks were observed along the plain areas, which caused extensive damage to lifeline structures such as roads and buildings (Fig. S2). From the observed EEEs, it is well established that the local geology and tectonics play an important role in earthquake damage distribution. The EEEs were distributed around a 100-km^2 area based on the post-earthquake observations along the mainland. The fault could have generated offshore faulting, but it has not been reported in any of the published documents. Thus, the total area for the EEE distribution of EEEs can be considered a minimum area. Therefore, the immediate post-earthquake analysis and reporting of the distribution of the EEEs are extremely important for seismic hazard analysis (Grützner et al., 2019; Naik et al., 2020a). Based on the distribution of EEEs and their dimension, the ESI-07 intensity was assessed for the 2018 Hualien earthquake following the INQUA ESI-07 intensity scale guideline (Michetti et al., 2007), and a detailed ESI-07 map (Fig. 9a–d) has been prepared. The ESI-07 intensity values of IX were given to Chihsingtan Beach, north Meilun, around Mt. Meilun, Dongdamen night market, and around the downtown of Hualien based on an observed 7.5 km long surface rupture with a sinistral offset of 10 cm–80 cm (Fig. 9a–d). The ESI-07 intensity values of VIII were assigned to places around Hualien port area, Huaxi Road, Jingmeli road, Jianguo road, the western part of Hualien city, Dongdamen night market, Beibin, Nanbin Park, Jian, and Soufeng area based on the observed liquefaction features (Fig. 8, Tables 1–4). Considering the surface rupture length of 7.5 km along the Milun fault and 6.2 km along the Lingding fault, the estimated epicentral intensity using Eq. (1) and Eq. (2) is I_0=IX-X and similar to the epicentral intensity estimated for the 1951 Hualien earthquake. The estimated intensity values based on the total length of the surface rupture are minimum because there is a possibility for the occurrences of offshore surface rupture, which is not included here due to a lack of observations.

The computed ESI-07 intensity was compared with the Central Weather Bureau (CWB) intensity scale (Taiwan) and MM intensity scale (USGS). The CWB scale used in the present work is prior to the 2020 CWB intensity scale as it was validated by the seismic station array network (CGS, 2018).

The MM and CWB intensity shows equal macroseismic intensity (MM VI-VII; CWB VII) for the 2018 Hualien earthquake. This may be due to both the scales having similar PGA ranges for intensity values I to VII. Comparing the traditional intensity scale (CWB and MM intensity) and the ESI-07 scale indicates that the ESI-07 intensity is two degrees higher than the other two scales (Fig. 5, Tables 1–4). The difference may be due to the traditional intensities used here being estimated from the estimated PGA and PGV, which were not calibrated according to the damage survey in Taiwan. On the other hand, the ESI -07-intensity map

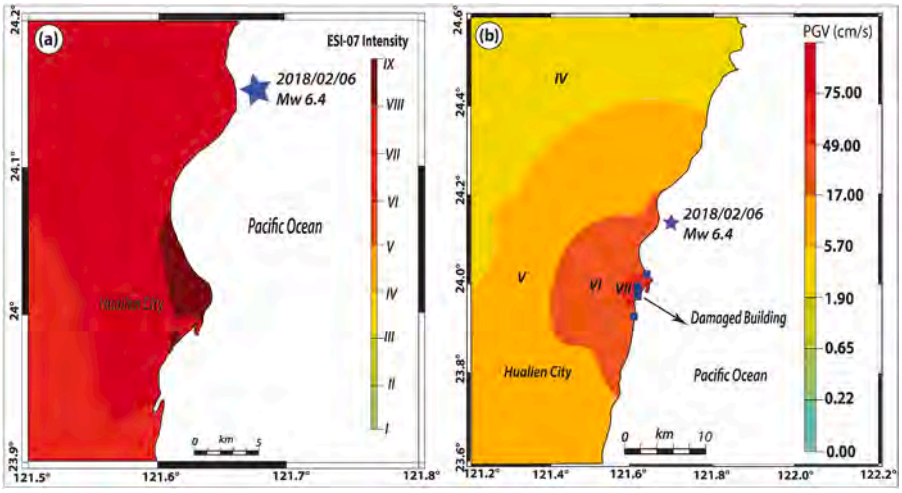

Fig. 10. Map showing the (a) ESI-07 ShakeMap for the 2018 Hualien earthquake based on the observed EEEs, (b) ShakeMap prepared considering the PGV which is the base of CWB intensity scale (modified from Wu et al., 2019).

shows a good relationship between the surface faulting and places with strong environmental effects. This could be the reason that traditional or instrumental intensity, which is mainly based on structural damage-based data and does not consider the local geology, underestimates the intensity values compared with the ESI-07 intensity scale.

The ShakeMaps generated (Fig. 10a) using the EEEs shows higher intensity around the location where higher ESI values were observed and vice-versa. The ShakeMaps were compared with the PGV-based ShakeMaps generated by Wu et al. (2019), which suggests a higher intensity of VII. The shape of the ShakeMaps contours prepared from the ESI-07 intensity values is very different from the PGV-based ShakeMaps contours and CWB intensity contours (Fig. 10b). This may be due to the exclusion of surface rupture in the ShakeMaps prepared by CWB and Wu et al. (2019). The ShakeMaps contour prepared from the EEEs shows that they are elongated along the surface rupture, which has maximum ESI-07 intensity. This infers that the EEEs should be complemented with the intensity estimations based on damaged structures or from instrumental data to have a better and more accurate macroseismic intensity.

7. Discussions

Around 450 data points, both qualitative and quantitative EEEs were compiled from different published sources for the 2018 Hualien earthquake, which are analyzed to estimate the ESI-07 intensity using the 12-degree macroseismic intensity scale proposed by Michetti et al. (2007). Most of the EEEs were concentrated along the previously marked tectonic faults and low-lying areas, suggesting that their occurrence was influenced by geological factors such as tectonic setting, geomorphology, and local site conditions (Fig. S2). The maximum ESI-07 intensity of I_0=IX was estimated for the 2018 Hualien earthquake. It is almost totally assigned to the locations strongly related to the presence of active fault and fault zones or sites proximal to the activated faults. This is another excellent example from Taiwan of how the presence of an active fault controls the localization of ground effects and seismic intensity. A similar observation was documented during the 1999 Chichi earthquake, where higher ESI 2007 scale values were concentrated on the fault trace (Ota et al., 2009). The assessed ESI-07 intensities were compared with the CWB and MM intensities. The ESI-07 intensity is commonly 3 degrees higher than the MM intensity. This might be due to the MM intensities (taken from USGS), based on the PGA and PGV, which are not calibrated according to the damage survey. Similar observations were seen in the CWB intensity, which indicates the ESI-07 intensity is two degrees higher than the CWB intensity (Fig. 9).

Despite this disagreement, the comparison of CWB intensity and MM intensity scales with the ESI-07 intensity (Fig. 9a–d) for the 2018 Hualien earthquake indicates that the traditional CWB and the MM scales underestimate the intensity at least for damaging earthquakes that have produced extensive EEEs in similar physical and anthropic environments. Therefore, EEEs and structural damages should be included in intensity determinations for future seismic hazard estimation.

The reassessment of macroseismic intensity for the 1951 Hualien earthquake, which caused extensive EEEs around the Hualien city (Fig. 4), allows us to understand and validate the role of local geology in seismic intensity estimation. The reassessment of the intensity indicates the seismic damage was controlled by the geological and geomorphological setting of the area rather than structural parameters. Based on the reported surface rupture length of ~9–10 km along the Milun Fault that has ruptured during both the 1951 and 2018 earthquakes, the estimated epicentral intensity is I_0 = X. This study demonstrates the applicability of the ESI-07 intensity scale to historical earthquakes with limited EEEs records. The estimated ESI-07 intensity for the historic 1951 Hualien earthquake is similar to the epicentral intensity estimated from the surface rupture length produced by the 2018 Hualien earthquake. This comparison manifests that the ESI-07 scale can presumably be applied to different earthquakes of similar dimensions in the same geological setting. Similar cases were reported from the Mediterranean region, where the 1867 earthquake along the Cephalonia Transform Fault was compared to the 2014 M = 6.0 event based on the geo-environmental effects, which suggested that the 1867 magnitude was overrated (Papathanassiou et al., 2017a, b). Also, Naik et al., 2020 suggested the importance of reassessment of the macroseismic intensity of the recent and historical earthquakes for a particular region, which may help the refinement of seismic hazard parameters by comparing the ESI-07 values for the 1819 Allahabund earthquake and the 2001 Bhuj earthquake. These previous studies and the present study highlight the significance of proper documentation of earthquakes and the environmental effects of maintaining consistency with historical earthquake catalogs. Consequently, the re-evaluation of seismic intensity using recorded EEEs for historical and recent earthquakes may help to reduce the uncertainty in attenuation relationships and improve seismic hazard assessments and maps for a particular region.

The CWB and MM intensity of the 2018 Hualien earthquake is two to three degrees lower than the ESI-07 intensity (Figs. 5 and 9). Most likely, the difference in the epicentral intensity assessed using both the traditional and ESI 2007 intensity scales is due to the introduction of modern seismic codes for new buildings. A similar result has already been obtained in other seismically active regions with relevant historical earthquake data (e.g., Ferrario et al., 2020).

The 2018 Hualien earthquake ESI-07 intensity was compared with other strike-slip earthquakes of similar magnitudes, such as the 2008 Andravida earthquake along NW Peloponnese, Greece (Mw = 6.4), 2008 Kultuk earthquake (Mw = 6.3), 2011–2012 Tuva earthquake in Russia (Mw = 6.6 and Mw = 6.7), 2011 Lorca earthquake, Spain (Mw = 5.1), 2014 Cephalonia (the Ionian Sea, western Greece) earthquake (M_w = 6.0) and 2015 Lefkada earthquake (Mw 6.4) (Berzhinskii et al., 2010; Silva et al., 2015a,b; Lekkas and Mavroulis, 2015; Papanikolaou and Melaki, 2017). Despite different tectonic and geological settings, all the listed earthquakes have generated similar ESI-07 values (ESI-07 = VIII) as the 2018 Hualien earthquake in Taiwan (ESI-07 = IX). The one degree of difference in ESI-07 values between the listed earthquakes and the 2018 Hualien earthquake may be due to the absence of primary effects in the case of later events. In contrast, the 2018 Hualien earthquake caused an extensive surface rupture. Also, the focal depth of the 2018 Hualien earthquake was much shallower than the other earthquakes listed here, which might have controlled the shaking intensity and for one degree higher ESI-07 values. However, comparing the ESI-07 values of these earthquake suggests that earthquakes of similar magnitude from different geo-tectonic settings can generate similar ground effects and produce similar ESI-07 values.

For a more accurate assesemnt of the seismic hazard and for reducing the uncertainty between the intensity-attenuation relationships for the recent earthquakes, it is important to develop a relationship between the earthquake magnitude and the ESI 2007 scale (Papanikolaou and Melaki, 2017; Velázquez-Bucio et al., 2021). To understand the relationship between the earthquake magnitude and the ESI-07 values for Taiwan, we have plotted the earthquake magnitude and the ESI-07 values of the 1935 Hsinchu-Taichung earthquake and 1999 Chichi earthquake reported by Ota et al., 2009 along with the 1951 Longitudinal valley earthquake and 2018 Hualien earthquake data reported in the present study (Fig. 11a). The following relationships provide the relationship between Taiwan's earthquake magnitude and ESI-07.

$$I_{o(ESI,\ 2007)} = f(M_w) \quad (3)$$

$$Io = 3.927\exp(0.1381M_w) \quad (4)$$

The developed relationship displays good correlations with R2 = 0.68 which can be improved with more case studies from Taiwan, which have a long history of damaging earthquakes.

The relationship between the earthquake magnitude and ESI-07 values for strike-slip fault earthquakes from Taiwan and other regions of the world was plotted to show whether the earthquake magnitude correlated with the ESI-07 values for strike-slip events (Fig. 11b). The correlation is provided as

$$Io = 1.9491\exp\ (0.2322\ M_w) \quad (5)$$

The developed correlation shows quite a good correlation with the earthquake magnitude and ESI-07 values with an R^2 value of 0.73 (Fig. 11b). The correlation suggests the earthquake of magnitude Mw 6–6.8 generates the ESI-07 values of VIII-IX, whereas the magnitude of Mw 6.9–7.7 generates the ESI-07 values of X-XI. Thus, the ESI-07 values estimated from the 2018 Hualien earthquake's ground effects are in agreement with other similar strike-slip events.

Also, the developed relationship was compared with the previous studies from the Mediterranean region (Papanikolaou and Melaki, 2017), which has a higher number of case studies to assess the relationship between the earthquake magnitude and ESI-07 values than other areas of the world (Fig. 11c). The developed correlation is in good agreement with the relationship suggested by Papanikolaou and Melaki (2017) (Fig. 11c). Papanikolaou and Melaki (2017) indicated that earthquakes of Mw = 6.3, Mw = 6.8, and Mw = 7.2 are expected to generate maximum ESI-07 values of VIII-IX, IX, and X for the Mediterranean region. In the case of Taiwan, the 1935 Hsinchu-Taichung earthquake of Mw = 7 and the 1999 Chichi earthquake of Mw = 7.7

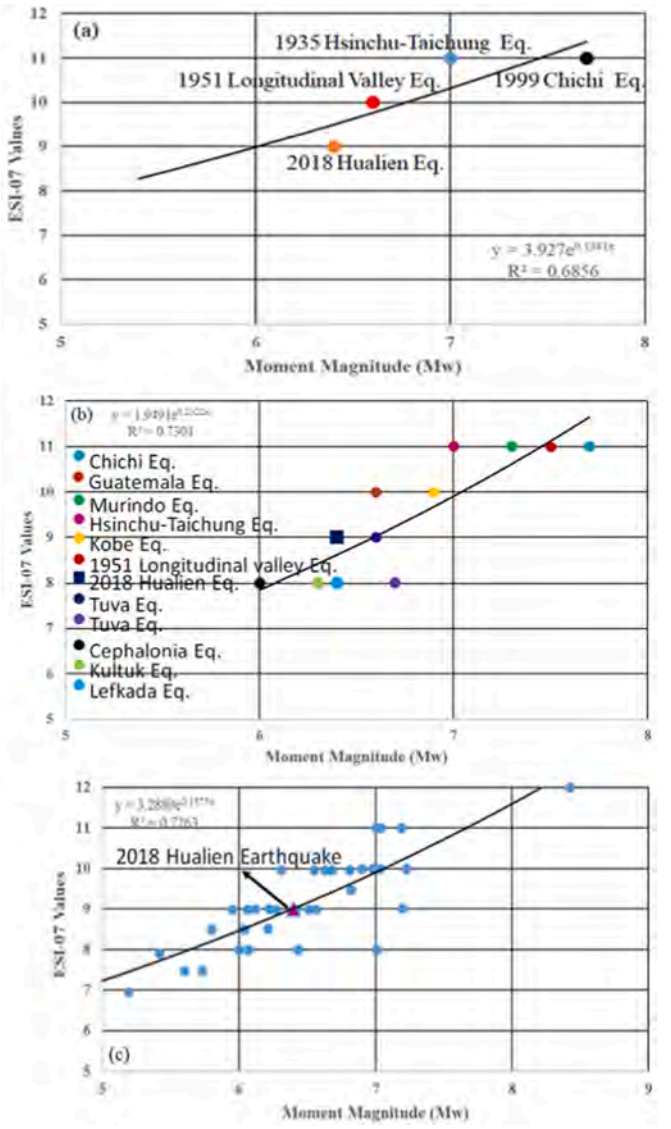

Fig. 11. (a) Diagram showing the correlation between the Mw and the ESI-07 scale in Taiwan. (b) Diagram showing the correlation between the Mw and the ESI 2007 scale for the earthquakes caused by strike slip fault including the two earthquakes considered in the present study. (c) Diagram showing the correlation between the Mw and ESI-07 scale for the Mediterranean region along with the 2018 Hualien earthquake in Taiwan. All the three diagrams show a good correlation between Mw and the ESI-07 scale.

have generated ESI-07 values of XI. In contrast, the 1951 Longitudinal valley earthquake (Mw = 6.6) and 2018 Hualien earthquake (Mw = 6.4) have caused ESI-07 values of X and IX, respectively, which is almost similar to the relationship suggested by Papanikolaou and Melaki (2017). This indicates that despite different faulting mechanisms, and tectonic and geological settings, earthquakes of similar magnitude generate similar ESI-07 intensity values. This testifies that the ESI-07 values depend on the earthquake's strength rather than reflecting an area's cultural setting and economic development. Hence it is recommended for a better seismic hazard scenario; the ESI-07 intensity scales should be complemented with the CWB intensity scale in Taiwan.

The relationship between the earthquake magnitude and ESI-07 value for different earthquakes in Taiwan and other areas of the world indicates that in-order to have an intensity-attenuation relationship for Taiwan, like the Mediterranean region, more case studies are required for the ESI-07 intensity estimation for historical and recent seismicity which was also previously suggested by Ota et al. (2009).

The ShakeMaps prepared from the EEEs show completely different contours than the ShakeMaps contours designed from the PGA or PGV values (Fig. 10). The intensity assignments vary by two degrees between the two ShakeMaps. The ShakeMaps contours prepared from the ESI-07 intensity values are elongated along the Hualien fault, which is in good agreement with the distribution of EEEs. In contrast, the ShakeMaps contours derived from instrumental PGA and PGV values are oval-shaped around the area where damaged buildings were observed. There was significant disagreement between the ShakeMaps prepared from the PGA or PGV and the distribution of EEEs. This indicates the ShakeMaps can be prepared considering the EEEs can be implemented with the instrumental data for a better seismic hazard assessment and hazard zonation studies in an urban area such as the epicentral area of the 2018 Hualien earthquake.

The ESI-07 intensity became one of the most crucial parameters in seismic hazard assessment as it offers information about the earthquake damage distribution to the natural environment. In countries like Taiwan, Japan, Korea, and China, because heterogeneous building codes are applied, and most seismic hazard maps were prepared from the structural damage data, the evaluation of the intensities using traditional intensity scales cannot be equally evaluated applied to the entire region. In such cases, the ESI-07 intensity scale offers higher resolution as it is solely based on natural effects and follows the same criteria for all the earthquakes worldwide despite different tectonic settings. In general, the ESI-07 intensity data from other regions can be compared and used in developing the empirical relationship between earthquake magnitude and ESI-07 intensity for earthquakes with different faulting types, which will enhance the resolution of seismic hazard assessment.

8. Conclusions

The seismic intensity of the 2018 Hualien earthquake, which was one of the most damaging earthquakes after the 1999 Chi-Chi earthquake in Taiwan, has been reassessed using the size and types of primary and secondary effects caused by the earthquake. An ESI-07 intensity map was compiled for the 2018 Hualien earthquake indicating the maximum intensity of IX, which will be helpful in the characterization of seismic hazards in and around Hualien city. The epicentral power of the historic 1951 Longitudinal valley fault earthquake ($I_0 = X$) is comparable to the epicentral intensity of the 2018 Hualien earthquake ($I_0 = IX\text{-}X$). Earthquake environmental effects of the 2018 and 1951 events have been systematically compared, which indicates that the ESI-07 assessment for the epicentral intensity was consistent.

The ESI-07 intensity values for the 1951 earthquake and 2018 Hualien earthquake are in good agreement with the ESI-07 values generated by similar magnitude strike-slip events from different geological and tectonic settings. This testifies that the ESI-07 values depend on the earthquake's strength rather than reflecting an area's cultural setting and economic development.

The study highlights the usefulness of EEEs in the seismic hazard assessment of epicentral areas (i.e., around Hualien city, eastern Taiwan) facing repeated damaging earthquakes in recent times.

The developed correlation between earthquake magnitude and ESI-07 for the 1951 Longitudinal valley and 2018 Hualien earthquake shoes good correlation with the other similar strike-slip events around the world.

The ShakeMaps map generated from the ESI-07 shows good agreement with the distribution of EEEs rather than structural parameters. This infers the ShakeMap prepared from the EEEs can predict better earthquake hazards and can be implemented with the instrumental intensity map for a more accurate seismic hazard assessment.

The current study suggests that the proper documentation of EEEs for other historical earthquakes in Taiwan can help to enhance the resolution of seismic hazard estimation, as mentioned by Ota et al. (2009). For accurate seismic hazard estimation on a regional or local scale, it is important to collect and document both qualitative and quantitative EEEs data for a proper seismic intensity estimation and ground motion data. In countries like Taiwan that are rapidly growing and developing accurate earthquake early warning systems, information about EEEs can play an important role in land use planning, sustainable development, and regional seismic hazard assessments.

Author contributions

Sambit Prasanajit Naik: Conceptualization, Methodology, Validation, Formal analysis and Writing the manuscript, preparing the illustrations. Asmita Mohanty: preparing illustrations, writing. Himanshu Mittal: Preparing ShakeMaps, ESI ShakeMaps and writing the manuscript. Alessandro Maria Michetti: Supervision, Reviewing. Sabina Porfido: Supervision, Reviewing. Benjamin Ming Yang: Preparation of ShakeMaps. Ohsang Gwon: preparing illustrations, writing. Young-Seog Kim: Supervision, Reviewing.

Data availability

Landsat data were taken from https://earthexplorer.usgs.gov/. The MM Intensity values were taken from https://earthquake.usgs.gov/earthquakes/eventpage/us700038c1/executive. CWB intensity values were taken from Central Weather Bureau, Seismological Division, Taiwan (https://scweb.cwb.gov.tw/en-us/earthquake/ShakeMaps/ee20180206235041620 22).

Declaration of competing interest

The authors declare that they have no known competing financial interests or personal relationships that could have appeared to influence the work reported in this paper.

Acknowledgements

The authors are thankful to Dr. Shao Yi-Huang (Huang et al., 2019) for providing field photographs. Also, the Authors are thankful to the Associate Editor of Terrestrial, Atmospheric and Oceanic Sciences Journal, Ms. Pei-Cin Jheng for allowing us to reproduce the field photographs provided by Dr. Shao Yi-Huang which is already used in Huang et al. (2019) showing surface ruptures of 2018 Hualien earthquake. The permission was granted via emails. All quantitative data used in this paper came from the published sources listed in the references. Authors are also thankful to Paolo Zimmaro, one of the contributor of Virtual Earthquake Reconnaissance Team (VERT) for allowing us to use some field photos of ground cracks from the VERT report.

Appendix A. Supplementary data

Supplementary data to this article can be found online at https://doi.org/10.1016/j.quaint.2022.10.009.

References

Ali, Z., Qaisar, M., Mahmood, T., Shah, M.A., Iqbal, T., Serva, L., Michetti, A.M., Burton, P.W., 2009. The Muzaffarabad, Pakistan, earthquake of 8 October 2005: surface faulting, environmental effects and macroseismic intensity. Geol. Soc. Lon. 316 (1), 155–172.

Audemard, F., Azuma, T., Baiocco, F., Baize, S., Blumetti, A.M., Brustia, E., Clague, J., Comerci, V., Esposito, E., Guerrieri, L., Gurpinar, A., Grutzner, C., Jin, K., Kim, Y.S., Kopsachilis, V., Lucarini, M., McCalpin, J., Michetti, A.M., Mohammadioun, N., Morner, N.A., Okumura, K., Ota, Y., Papathanassiou, G., Pavlides, S., Perez-Lopez, R., Porfido, S., Reicherter, K., RodriguezPascua, M.A., Roghozin, E., Scaramella, A., Serva, L., Silva, P.G., Sintubin, M., Tatevossian, R., Vittori, E., 2015. Earthquake environmental effects for seismic hazard assessment: the ESI intensity scale and the EEE catalogue. In: Guerrieri, Luca (Ed.), Memoire Destrictive Della Carta Geologica D'Italia, XCVII (2015) ISPRA Servizio Geologico D' Italia, p. 181.

Berzhinskii, Y.A., Ordynskaya, A.P., Gladkov, A.S., Lunina, O.V., Berzhinskaya, L.P., Radziminovich, N.A., Radziminovich, Y.B., Imayev, V.S., Chipizubov, A.V., Smekalin, O.P., 2010. Application of the ESI-2007 scale for estimating the intensity

of the Kultuk earthquake, August 27, 2008 (south Baikal). Seism. Instrum. 46 (4), 307–324.
Caccavale, M., Sacchi, M., Spiga, E., Porfido, S., 2019. The 1976 Guatemala earthquake: ESI scale and Probabilistic/Deterministic seismic hazard analysis approaches. Geosci. 9 (9), 403.
Central Geological Survey (CGS), 2018. Geological Investigation Report of 20180206 Hualien Earthquake. Central Geological Survey, Ministry of Economic Affairs, Taipei, Taiwan (in Chinese).
Chang, C.P., Chen, K.S., Chung, L.H., Yen, J.Y., Shih, T.S., 2006. Active fault propagation in metropolitan Hualien of eastern Taiwan: observed by radar interferometry and field investigation. In: Int. Workshop: Appl. Of SAR Data in Taiwan, Taoyuan, Taiwan.
Chen, C.Y., Lee, J.C., Chen, Y.G., Chen, R.F., 2014a. Campaigned GPS on present-day crustal deformation in northernmost Longitudinal Valley preliminary results, Hualien Taiwan. Terr. Atmos. Ocean Sci. 25 (3), 337–357.
Chen, S.K., Chan, Y.C., Hu, J.C., Kuo, L.C., 2014b. Current crustal deformation at the junction of collision to subduction around the Hualien area, Taiwan. Tectonophysics 617, 58–78.
Chen, P.F., Chen, Y.L., Su, P.-L., Peng, Y.-D., Chen, L.-F., 2019. Understanding the 6 February 2018, Hualien earthquake sequence through catalog compilation. Terr. Atmos. Ocean Sci. 30, 399–409.
Cheng, S.N., Yeh, Y.T., Yu, M.S., 1996. The 1951 Taitung earthquake in Taiwan. J. Geol. Soc. China 39 (3), 267–285.
Chung, L.H., 2003. Surface Rupture Re-evaluation of the 1951 Earthquake Sequence in the Middle Longitudinal Valley and Neotectonic Implications. M.S. thesis. National Taiwan University, Taipei, p. 138pp (in Chinese with English Abstract).
Chunga, K., Livio, F., Mulas, M., Ochoa-Cornejo, F., Besenzon, D., Ferrario, M.F., Michetti, A.M., 2018. Earthquake ground effects and intensity of the 16 April 2016 Mw 7.8 Pedernales, Ecuador, earthquake: implications for the source characterization of large subduction earthquakes. Bull. Seismol. Soc. Am. 108, 3384–3397.
Coburn, A., Spence, R., 2003. Earthquake Protection. John Wiley & Sons, ISBN 978-0-470-85517-1.
Ferrario, M.F., Livio, F., Serra Capizzano, S., Michetti, A.M., 2020. Developing the first Intensity Prediction Equation based on the Environmental Scale Intensity: a case study from strong normal faulting earthquakes in the Italian Apennines. Seism. Res. Lett. XX 1–13.
Fischer, E., Hakhamaneshi, M., Yoo, D., Haro, A.G., Joshi, V., Pérez-Irizarry, Á., Gartner, M., Ma, X., Lee, J.S., Paul, N., Sanchez, D., Fiszman, E., Zimmaro, P., Nikl, T.R., 2018. Virtual Earthquake Reconnaissance Team (VERT): Immediate Response to "Hualien. Taiwan" Earthquake.
Giner-Robles, J.L., Silva, P.G., Elez, J., Rodríguez-Pascua, M.A., Perez-Lopez, R., Rodríguez-Escudero, E., 2015. Relationships between the ESI-07 scale and expected PGA values from the analysis of two historical earthquakes (≥ VIII EMS) in East Spain: tavernes 1396 AD and Estubeny 1748 AD events. April. In: Proceedings of the 6th International INQUA Meeting in Paleoseismology, Active Tectonics and Archaeoseismology, Pescina, Fucino Basin, Italy, pp. 19–24.
Grandori, G., Drei, A., Perotti, F., Tagliani, A., 1991. Macroseismic intensity versus epicentral distance: the case of Central Italy. Tectonophysics 193, 165–171.
Grützner, C., Walker, R., Ainscoe, E., Elliott, A., Abdrakhmatov, K., 2019. Earthquake environmental effects of the 1992 MS7. 3 Suusamyr earthquake, Kyrgyzstan, and their implications for Paleo-earthquake studies. Geosci. 9 (6), 271.
Guerrieri, L., Blumetti, A.M., Esposito, E., Michetti, A.M., Porfido, S., Serva, L., Tondi, E., Vittori, E., 2009. Capable faulting, environmental effects and seismic landscape in the area affected by the 1997 Umbria–Marche (Central Italy) seismic sequence. Tectonophysics 476 (1–2), 269–281.
Guerrieri, L., Amanti, M., Galluzzo, F., Leoni, G., Michetti, A.M., Roma, M., Vittori, E., Central Italy Earthquake Working Group, 2016. Geological Effects of the August 24, 2016, Central Italy Earthquake: Preliminary Application of the ESI07 Intensity Scale.
Heddar, A., Beldjoudi, H., Authemayou, C., SiBachir, R., Yelles-Chaouche, A., Boudiaf, A., 2016. Use of the ESI-2007 scale to evaluate the 2003 Boumerdès earthquake (North Algeria). Ann. Geophys. 59, 0211.
Hsu, M.T., 1961. Seismicity of Taiwan (Formosa), vol. 39. Bull. Earthq. Res. Inst. Tokyo University, pp. 831–847.
Hsu, T.L., 1962. Recent faulting in the longitudinal valley of eastern Taiwan. Proc. Geol. Soc. China Mem. 1, 95–102.
Hsu, M.T., 1979. Seismology. Lee-Ming Culture Publication Company, Taipei, Taiwan, pp. 16–26 (in Chinese).
Hsu, Y.C., Chang, C.P., Yen, J.Y., Kuo, C.H., Wang, C.C., 2019. Investigating the structure of the Milun fault from surface ruptures of the 2018 Hualien Earthquake. Terr. Atmos. Ocean Sci. 30, 337–350.
Huang, K.C., Kao, H., Wu, Y.M., 2000. The Determination of the ML-Mw in Taiwan. Proceedings of the 8th Annual Meeting of Geophysical Society of China, Taipei city, Taiwan, pp. 193–201.
Huang, S.Y., Yen, J.Y., Wu, B.L., Yen, I.C., Chuang, R.Y., 2019. Investigating the Milun Fault: the co-seismic surface rupture zone of the 2018/02/06 M L 6.2 Hualien earthquake, Taiwan. Terr. Atmos. Ocean Sci. 30 (3), 1–25.
Huayong, N., Hua, G., Yanchao, G., Blumetti, A.M., Comerci, V., Di Manna, P., Guerrieri, L., Vittori, E., 2019. Comparison of Earthquake Environmental Effects and ESI intensities for recent seismic events in different tectonic settings: Sichuan (SW China) and Central Apennines (Italy). Eng. Geol. 258, 105149.
ISPRA-INQUATERPRO. EEE catalogue. INQUA TERPRO Project #0811, ISPRA –geological survey of Italy working group (online). Available: http://www.eeecatalog.sinanet.apat.it/terremoti/index.php.
Klinger, Y., 2010. Relation between continental strike-slip earthquake segmentation and thickness of the crust. J. Geophys. Res. 115 (B7).
Ko, Y.Y., Hsu, S.-Y., Yang, H.C., Lu, C.C., Hwang, Y.W., Liu, C.H., Hwang, J.H., 2019. Soil liquefaction and ground settlements in 6 February 2018 Hualien, Taiwan, earthquake. Seismol Res. Lett. 90 (1), 51–59.
Kuo, Y.T., Wang, Y., Hollingsworth, J., Huang, S.Y., Chuang, R.Y., Lu, C.H., Hsu, Y.C., Tung, H., Yen, J.Y., Chang, C.P., 2019. Shallow fault rupture of the Milun fault in the 2018 Mw 6.4 Hualien earthquake: a high-resolution approach from optical correlation of Pléiades satellite imagery. Seismol Res. Lett. 90 (1), 97–107.
Kuo-Chen, H., Guan, Z.K., Sun, W.F., Jhong, P.Y., Brown, D., 2019. Aftershock sequence of the 2018 M w 6.4 Hualien earthquake in eastern Taiwan from a dense seismic array data set. Seismol Res. Lett. 90 (1), 60–67.
Lee, Y.-H., Chen, G.-T., Rau, R.-J., Ching, K.E., 2008. Co-seismic displacement and tectonic implication of 1951 Longitudinal Valley earthquake sequence, eastern Taiwan. J. Geophys. Res. 113 (B04305).
Legendre, C.P., Tseng, T.L., Mittal, H., Hsu, C.H., Karakhanyan, A., Huang, B.S., 2017. Complex wave propagation revealed by peak ground velocity maps in the Caucasus Area. Seismol Res. Lett. 88 (3), 812–821.
Lekkas, E.L., 2010. The 12 may 2008 M w 7.9 Wenchuan, China, earthquake: macroseismic intensity assessment using the EMS-98 and ESI 2007 scales and their correlation with the geological structure. Bull. Seismol. Soc. Am. 100 (5B), 2791–2804.
Lekkas, E.L., Mavroulis, S.D., 2015. Earthquake environmental effects and ESI 2007 seismic intensities of the early 2014 Cephalonia (Ionian Sea, western Greece) earthquakes (January 26 and February 3, Mw 6.0). Nat. Hazards 78 (3), 1517–1544.
Lin, M.S., Hsiao, C.L., 1998. The strike-slip fault system in the Milun Tableland. Res. of Eastern Taiwan 3, 13–30 (in Chinese).
Lin, C.W., Chen, W.S., Liu, Y.C., Chen, P.T., 2009. Active Faults of Eastern and Southern Taiwan. Central Geological Survey, Taiwan.
Lin, Y.S., Chuang, R.Y., Yen, J.Y., Chen, Y.C., Kuo, Y.T., Wu, B.L., Huang, S.Y., Yang, C.J., 2019. Mapping surface breakages of the 2018 Hualien earthquake by using UAS photogrammetry. Terr. Atmos. Ocean Sci. 30 (3), 351–366.
Lin, J.L., Kuo, C.H., Chang, Y.W., Chao, S.H., Li, Y.A., Shen, W.C., Yu, C.H., Yang, C.Y., Lin, F.R., Hung, H.H., Chen, C.C., 2020. Reconnaissance and learning after the February 6, 2018, earthquake in Hualien, Taiwan. Bull. Earthq. Eng. 18, 4725–4754.
Liu, K.S., Tsai, Y.B., Chen, K.P., 2013. Estimation of seismic hazard potential in Taiwan based on ShakeMaps. Nat. Hazards 69 (3), 2233–2262.
Liu-Zeng, J., Wang, P., Zhang, Z., Li, Z., Cao, Z., Zhang, J., Yuan, X., Wang, W., Xing, X., 2017. Liquefaction in western Sichuan basin during the 2008 Mw 7.9 Wenchuan earthquake, China. Tectonophysics 694, 214–238.
Lo, C.L., Chang, E.T.Y., Chao, B.F., 2013. Relocating the historical 1951 Hualien earthquake in eastern Taiwan based on tide gauge record. Geophys. J. Int. 192 (2), 854–860.
McClay, K., Bonora, M., 2001. Analog models of restraining step overs in strike-slip fault systems. Am. Assoc. Petrol. Geol. Bull. 85 (2), 233–260.
McGuire, R.K., 1993. Computations of seismic hazard. Ann. Geofisc. 36, 181–200.
Michetti, A.M., Esposito, E., Gurpinar, A., Mohammadioun, B., Mohammadioun, J., Porfido, S., Rogozhin, E., Serva, L., Tatevossian, R., Vittori, E., Audemard, F., Comerci, V., Marco, S., McCaplin, J., Morner, N.A., 2004. The INQUA Scale: an Innovative Approach for Assessing Earthquake Intensities Based on Seismically Induced Ground Effects in Natural Environment Roma Sp. Paper Mem. Descr, LXVII. Carta Geologica d' Italia, p. 118, 2004.
Michetti, A.M., Esposito, E., Guerrieri, L., Porfido, S., Serva, L., Tatevossian, R., Vittori, E., Audemard, F., Azuma, T., Clague, J., Comerci, V., 2007. Environmental seismic intensity scale-ESI 2007. Mem. Descri. Della Carta Geol. d'Ital. 74, 41.
Mittal, H., Wu, Y.M., Lin, T.L., Legendre, C.P., Gupta, S., Yang, B.M., 2019. Time-dependent ShakeMaps map for Uttarakhand Himalayas, India, using recorded earthquakes. Acta Geophys. 67, 753–763. https://doi.org/10.1007/s11600-019-00281-7.
Mittal, H., Yang, B.M., Tseng, T.L., Wu, Y.M., 2021. Importance of real-time PGV in terms of lead-time and shakemaps: results using 2018 ML 6.2 & 2019 ML 6.3 Hualien, Taiwan earthquakes. J.Asian Ear. Sc. 220, 104936.
Mosquera-Machado, S., Lalinde-Pulido, C., Salcedo-Hurtado, E., Michetti, A.M., 2009. Ground effects of the 18 October 1992, Murindo earthquake (NW Colombia), using the environmental seismic intensity scale (ESI 2007) for the assessment of intensity. Geol. Soc. Lon. 316 (1), 123–144.
Naik, S.P., Mohanty, A., Porfido, S., Tuttle, M., Gwon, O., Kim, Y.S., 2020a. Intensity estimation for the 2001 Bhuj earthquake, India on ESI-07 scale and comparison with historical 16th June 1819 Allah Bund earthquake: a test of ESI-07 application for intraplate earthquakes. Quat. Int. 536, 127–143.
Naik, S.P., Gwon, O., Porfido, S., Park, K., Jin, K., Kim, Y.S., Kyung, J.B., 2020b. Intensity reassessment of the 2017 Pohang earthquake Mw= 5.4 (South Korea) using ESI-07 scale. Geosc 10 (11), 471.
Nappi, R., Gaudiosi, G., Alessio, G., De Lucia, M., Porfido, S., 2017. The environmental effects of the 1743 Salento earthquake (Apulia, southern Italy): a contribution to seismic hazard assessment of the Salento Peninsula. Nat. Hazards 86 (2), 295–324.
Ng, S.M., Ando, M., Wen, K.L., Huang, J.Y., Hu, J.C., 2011. Earthquake Intensity scale problem in Taiwan as revealed by damaging events in past decade. Geophys. Res. Abstr. 13, EGU2011–5372, 2011 EGU General Assembly 2011.
Ota, Y., Azuma, T., Lin, Y.N.N., 2009. Application of INQUA environmental seismic intensity scale to recent earthquakes in Japan and Taiwan. Geol. Soc. Lon. 316 (1), 55–71.
Papanikolaou, I.D., 2011. Uncertainty in intensity assignment and attenuation relationships: how seismic hazard maps can benefit from the implementation of the Environmental Seismic Intensity scale (ESI 2007). Quat. Int. 242 (1), 42–51.
Papanikolaou, I.D., Melaki, M., 2017. The Environmental Seismic Intensity Scale (ESI 2007) in Greece, addition of new events and its relationship with magnitude in

Greece and the Mediterranean; preliminary attenuation relationships. Quat. Int. 451, 37–55.
Papanikolaou, I.D., Papanikolaou, D.I., Lekkas, E.L., 2009. Advances and limitations of the Environmental Seismic Intensity scale (ESI 2007) regarding near-field and far-field effects from recent earthquakes in Greece: implications for the seismic hazard assessment. Geol. Soc. Lon. 316 (1), 11–30.
Papathanassiou, G., Valkaniotis, S., Ganas, A., 2017a. Evaluation of the macroseismic intensities triggered by the January/February 2014 Cephalonia,(Greece) earthquakes based on ESI-07 scale and their comparison to 1867 historical event. Quat. Int. 451, 234–247.
Papathanassiou, G., Valkaniotis, S., Ganas, A., Grendas, N., Kollia, E., 2017b. The November 17th, 2015 Lefkada (Greece) strike-slip earthquake: field mapping of generated failures and assessment of macroseismic intensity ESI-07. Eng. Geol. 220, 13–30.
Pettenati, F., Sirovich, L., Cavallini, F., 1999. Objective treatment and synthesis of macroseismic intensity data sets using tessellation. Bull. Seismol. Soc. Am. 89, 1203–1213.
Porfido, S., Esposito, E., Vittori, E., Tranfaglia, G., Guarrieri, L., Pece, R., 2007. Seismically induced ground effects of the 1805, 1930 and 1980 earthquakes in the Southern Apennines (Italy. Boll. Soc. Geol. It. (Ital. J. Geosci.) 126 (2), 333–346.
Porfido, S., Nappi, R., De Lucia, M., Gaudiosi, G., Alessio, G., Guerrieri, L., 2015a. The ESI scale, an ethical approach to the evaluation of seismic hazards. Geophs Res Abs 17. EGU2015-11732-2.
Porfido, S., Esposito, E., Sacchi, M., Molisso, F., Mazzola, S., 2015b. Impact of ground effects for an appropriate mitigation strategy in seismic area: the example of Guatemala 1976 earthquake. In: Lollino, G., Giordan, D., Crosta, G., Corominas, J., Azzam, R., Wasowski, J., Sciarra, N. (Eds.), Engineering Geology for Society and Territory, vol. 2, pp. 703–708.
Porfido, S., Alessio, G., Gaudiosi, G., Nappi, R., 2020. New Perspectives in the Definition/evaluation of seismic hazard through analysis of the environmental effects induced by earthquakes. Geosciences 10 (2), 58, 2020.
Reicherter, K., Michetti, A.M., Barroso, P.S., 2009. Paleoseismology: historical and prehistorical records of earthquake ground effects for seismic hazard assessment. Geol. Soc. Lon. 316 (1), 1–10.
Sanchez, J.J., Maldonado, R.F., 2016. Application of the ESI 2007 scale to two large earthquakes: south Island, New Zealand (2010 M w 7.1), and Tohoku, Japan (2011 M w 9.0). Bull. Seismol. Soc. Am. 106 (3), 1151–1161.
Serva, L., 1994. Ground effects in the intensity scales. Terra. Nova 6, 414–416.
Serva, L., Blumetti, A.M., Esposito, E., Guerrieri, L., Michetti, A.M., Okumura, K., Porfido, S., Reicherter, K., Silva, P.G., Vittori, E., 2015. Earthquake Environmental Effects, Intensity and Seismic Hazard Assessment: the Lesson of Some Recent Large Earthquakes. Memo. Desc. Della Carta Geol. D'Italia; ISPRA Istituto Superiore per la Protezione e la Ricerca Ambientale, Rome, Italy.
Serva, L., Vittori, E., Comerci, V., Esposito, E., Guerrieri, L., Michetti, A.M., Mohammadioun, B., Mohammadioun, G.C., Porfido, S., Tatevossian, R.E., 2016. Earthquake hazard and the environmental seismic intensity (ESI) scale. Pure Appl. Geophys. 173 (5), 1479–1515.
Shyu, J.B.H., Sieh, K., Chen, Y.G., Liu, C.S., 2005. Neotectonic architecture of Taiwan and its implications for future large earthquakes. J. Geophys. Res. 110 (B8).
Shyu, J.B.H., Chung, L.H., Chen, Y.G., Lee, J.C., Sieh, K., 2007. Re-evaluation of the surface ruptures of the November 1951 earthquake series in eastern Taiwan, and its neotectonic implications. J. Asian Earth Sci. 31 (3), 317–331.
Shyu, J.B.H., Sieh, K., Chen, Y.G., Chuang, R.Y., Wang, Y., Chung, L.H., 2008. Geomorphology of the southernmost Longitudinal Valley fault: implications for evolution of the active suture of eastern Taiwan. Tecton 27 (1), 1–22.
Shyu, J.B.H., Chuang, Y.R., Chen, Y.L., Lee, Y.R., Cheng, C.T., 2016. A new on-land Seismogenic structure source database from the Taiwan earthquake model (TEM) Project for seismic hazard analysis of Taiwan. Terr. Atmos. Ocean Sci. 27 (3), 311–323.
Silva, P.G., Guerrieri, L., Michetti, A.M., 2015a. Intensity Scale ESI 2007 for Assessing Earthquake Intensities. Springer Encyclopaedia of Earthquake Engineering, Berlin (Germany), pp. 1–20. Springer-Verlag.
Silva, P.G., Pérez-López, R., Rodríguez-Pascua, M.A., Roquero, E., Giner-Robles, J.L., Huerta, P., Martínez-Graña, A., Bardají, T., 2015b. Macroseismic analysis of slope movements triggered by the 2011 Lorca Earthquake (Mw 5.1): application of the ESI-07 scale. Geogaceta 57, 35–38.
Silva, P.G., Elez, J., Giner-Robles, J.L., Rodríguez-Pascua, M.A., Pérez-López, R., Roquero, E., Bardají, T., Martínez-Graña, A., 2017. ESI-07 ShakeMaps for instrumental and historical events in the Betic Cordillera (SE Spain): an approach based on geological data and applied to seismic hazard. Quat. Int. 451, 185–208.
Taiwan Weather Bureau, 1952. The 1951 Earthquake Report. Taiwan Weather Bureau, Taipei, p. 83pp (in Chinese).
Tatevossian, R.E., Mokrushina, N.G., Ovsyuchenko, A.N., Tatevossian, T.N., 2010. Geological and macroseismic effects of the Muya, 1957 earthquake and palaeoearthquakes in Baikal region. Seism. Instrum. 46 (2), 152–176.
Teng, L.S., 1990. Late Cenozoic arc-continent collision in Taiwan. Tectonophysics 183, 57–76.
Theunissen, T., Font, Y., Lallemand, S., Liang, W.T., 2010. The largest instrumentally recorded earthquake in Taiwan: revised location and magnitude, and tectonic significance of the 1920 event. Geophys. J. Int. 183 (3), 1119–1133.
Trifunac, M.D., Brady, A.G., 1975. On the correlation of seismic intensity scales with the peaks of recorded ground motion. Bull. Seismol. Soc. Am. 65, 139–162.
Tsai, S.F., 1987. The May 1986 Hualien Earthquake Sequence and its Relation with the Regional Tectonic Stress. M.S. Thesis. Institute of Geology, National Taiwan University.
Tsai, Y.B., Yu, T.M., Chao, H.L., Lee, C.P., 2001. Spatial distribution and age dependence of human-fatality rates from the Chi-Chi, Taiwan, Earthquake of 21 September 1999. Bull. Seismol. Soc. Am. 91, 1298–1309.
Tsai, M.C., Yu, S.B., Shin, T.C., Kuo, K.W., Leu, P.L., Chang, C.H., Ho, M.Y., 2015. Velocity field derived from Taiwan continuous GPS array (2007-2013). Terr. Atmos. Ocean Sci. 26 (5), 527–556.
Tuttle, M.P., Hartleb, R., Wolf, L., Mayne, P.W., 2019. Paleoliquefaction studies and the evaluation of seismic hazard. Geosci. 9, 311.
Velázquez-Bucio, M.M., Ferrario, M.F., Muccignato, E., Porfido, S., Sridharan, A., Chunga, K., Livio, F., Gopalan, S., Michetti, A.M., 2021. Environmental effects caused by the Mw 8.2, September 8, 2017, and Mw 7.4, June 23, 2020, Chiapas-Oaxaca (Mexico) subduction events: comparison of large intraslab and interface earthquakes. Quat. Int. https://doi.org/10.1016/j.quaint.2021.11.028.
Wald, D.J., Quitoriano, V., Heaton, T.H., Kanamori, H., Scrivner, C.W., Worden, C.B., 1999. TriNet "ShakeMapsMaps": rapid generation of instrumental ground motion and intensity maps for earthquakes in southern California. Earthq. Spectra 15, 537–555.
Wald, D.J., Worden, B.C., Quitoriano, V., Pankow, K.L., 2005. ShakeMap Manual: Technical Manual, User's Guide, and Software Guide. No. 12-A1).
Wang, J.-H., Kuo, H.-C., 1995. A catalogue of M >=7 Taiwan earthquakes (1900–1994). J. Geol. Soc. China 38 (2), 95–106.
Wen, Y.-Y., Wen, S., Lee, Y.-H., Ching, K.-E., 2019. The kinematic source analysis for 2018 Mw 6.4 Hualien, Taiwan earthquake. Terr. Atmos. Ocean Sci. 30, 377–387.
Wood, H.O., Neumann, F., 1931. Modified Mercalli intensity scale of 1931. Bull. Seismol. Soc. Am. 21, 277–283.
Wu, Y.M., Teng, T.L., Shin, T.C., Hsiao, N.C., 2003. Relationship between peak ground acceleration, peak ground velocity, and intensity in Taiwan. Bull. Seismol. Soc. Am. 93 (1), 386–396.
Wu, Y.M., Liang, W.T., Mittal, H., Chao, W.A., Lin, C.H., Huang, B.S., Lin, C.M., 2016. Performance of a low-cost earthquake early warning system (P-alert) during the 2016 ML 6.4 Meinong (Taiwan) earthquake. Seismol Res. Lett. 87, 1050–1059.
Wu, Y.M., Mittal, H., Huang, T.C., Yang, B.M., Jan, J.C., Chen, S.K., 2019. Performance of a low-cost earthquake early warning system (P-Alert) and shake map production during the 2018Mw 6.4 Hualien (Taiwan) earthquake. Seismol Res. Lett. 90 (1), 11.
Yang, Y.C., 1953. Earthquakes in Hualien in the latest 41 years. Hualien Lit 1, 67–71, 1953.
Yang, Y.-H., Hu, J.-C., Tung, H., Tsai, M.-C., Chen, Q., Xu, Q., Zhang, Y.-J., Zhao, J.-J., Liu, G.-X., Xiong, J.-N., Wang, J.-Y., Yu, B., Chiu, C.-Y., Su, Z., 2018. Co- seismic and Postseismic fault models of the 2018 Mw 6.4 Hualien earthquake occurred in the junction of collision and subduction boundaries offshore eastern Taiwan. Rem. Sens. 10, 1372.
Yang, B.M., Huang, T.C., Wu, Y.M., 2018. ShakingAlarm: a nontraditional regional earthquake early warning system based on time-dependent anisotropic peak ground-motion attenuation RelationshipsShakingAlarm: a nontraditional regional EEWS. Bull. Seismol. Soc. Am. 108, 1219–1230.
Yang, B.M., Mittal, H., Wu, Y.-M., 2021. Real-time production of PGA, PGV, intensity, and Sa ShakeMaps using dense MEMS-based Sensors in Taiwan. Senshokutai 21, 943.
Yu, S.B., Kuo, L.C., 2001. Present-day crustal motion along the longitudinal valley fault, eastern taiwan. Tectonophysics 333, 199–217.